Structure of mammalian V-ATPase with the TLDc domain protein mEAK7 bound

Yong Zi Tan[1,^,&], Yazan M. Abbas[1], Jing Ze Wu[2,3], Di Wu[4,5], Geoffrey G. Hesketh[6], Stephanie A. Bueler[1], Anne-Claude Gingras[6,7], Carol V. Robinson[4,5], Sergio Grinstein[2,3], John L. Rubinstein[1,3,8,*]

[1]Molecular Medicine Program, The Hospital for Sick Children Research Institute, Toronto, ON M5G 0A4, Canada.
[2]Program in Cell Biology, The Hospital for Sick Children, Toronto, ON M5G 0A4, Canada.
[3]Department of Biochemistry, University of Toronto, Toronto, ON M5S 1A8, Canada.
[4]Physical and Theoretical Chemistry Laboratory, University of Oxford, Oxford, OX1 3QZ, UK.
[5]Kavli Institute for Nanoscience Discovery, University of Oxford, Oxford, OX1 3QU, UK.
[6]Lunenfeld-Tanenbaum Research Institute, Sinai Health System, Toronto, ON M5G 1X5, Canada.
[7]Department of Molecular Genetics, University of Toronto, Toronto, ON M5S 1A8, Canada.
[8]Department of Medical Biophysics, University of Toronto, Toronto, ON M5G 1L7, Canada.
^Current address: Department of Biological Sciences, National University of Singapore, 16 Science Drive 4, Singapore 117558, Singapore.
[&]Current address: Disease Intervention Technology Laboratory, Immunos, Agency for Science, Technology and Research (A*STAR), 8A Biomedical Grove, Singapore 138648, Singapore.
* Correspondence to: john.rubinstein@utoronto.ca

Abstract

V-ATPases are rotary proton pumps that serve as signaling hubs, with numerous proposed binding partners in cells. We used cryoEM to detect endogenous proteins that associate with V-ATPase from porcine kidney. A super-stoichiometric copy of subunit C was found in ~3% of complexes, while an additional ~1.6% of complexes bound mEAK7, a protein with proposed roles in dauer formation in nematodes and mTOR signaling in mammals. High-resolution cryoEM of porcine kidney V-ATPase with recombinant mEAK7 shows that mEAK7's TLDc domain, which is found in other proteins proposed to bind V-ATPase, interacts with V-ATPase's stator while its C-terminal α helix binds V-ATPase's rotor. This crosslink would be expected to inhibit rotary catalysis. However, exogenous mEAK7 does not inhibit purified V-ATPase activity and mEAK7 overexpression in cells does not alter lysosomal or phagosomal pH. Instead, cryoEM suggests that interaction of mEAK7 with V-ATPase is disrupted by ATP-induced rotation of the rotor. Together, these results reveal how TLDc domains bind V-ATPases and suggest that V-ATPase binding proteins can form labile interactions that are sensitive to the enzyme's activity.

Introduction

Vacuolar-type adenosine triphosphatases (V-ATPases) are large, membrane-embedded protein complexes that function as proton pumps in eukaryotic cells. V-ATPase activity is essential for acidification of numerous intracellular compartments including endosomes, lysosomes, and secretory vesicles (Forgac, 2007). In some specialized cells V-ATPases pump protons from the cytoplasm to the extracellular environment, enabling activities ranging from acidification of the distal renal tubule lumen by kidney intercalated cells to dissolution of bone minerals by osteoclasts (Eaton et al., 2020). The enzyme consists of a soluble catalytic V_1 region that hydrolyzes ATP and a membrane-embedded V_O region responsible for proton pumping. ATP hydrolysis in the A_3B_3 subcomplex of the V_1 region induces rotation of the rotor subcomplex, which contains subunits D, F, d, and a ring of membrane-embedded c subunits (Vasanthakumar and Rubinstein, 2020). In the mammalian V_O region, the c-ring is comprised of nine c subunits and a single c″ subunit, with subunits ATP6AP1/Ac45 and ATP6AP2/PRR trapped inside the ring (Abbas et al., 2020). Rotation of the c-ring against subunit a drives proton translocation through the membrane. Three peripheral stalks, each consisting of heterodimers of subunits E and G, hold subunit a, along with subunits e and f (known as RNAseK in mammals) (Abbas et al., 2020), stationary relative to the rotor. Proton pumping by V-ATPase is regulated by the reversible dissociation of the V_1 and V_O regions (Kane, 1995; Sumner et al., 1995), with subunit H inhibiting of ATP hydrolysis in the detached V_1 region (Parra et al., 2000) and subunit C separating from V_1 following dissociation (Tabke et al., 2014).

V-ATPases interact with other proteins in the cell (Lee et al., 1999; Lu et al., 2001). In particular, V-ATPases are increasingly recognized as having important roles in signaling pathways such Wnt (Cruciat et al., 2010), mTORC1 (Zoncu et al., 2011), and Notch (Vaccari et al., 2010; Yan et al., 2009), with each pathway involving different proteins interacting with the enzyme. Further, analysis of V-ATPase from kidney tissue identified ARHGEF7, DMXL1, EZR, NCOA7, OXR1, RPS6KA3, SNX27, and nine-subunits of the CCT complex as V-ATPase associated proteins (Merkulova et al., 2015). Two of these proteins, NCOA7 and OXR1, contain TLDc domains and are believed to protect against oxidative stress (Finelli et al., 2016). These numerous roles and interactions involving V-ATPases suggest that in cells the enzyme may be found in complex with many different binding partners. However, despite cryoEM structures having been determined from endogenous V-ATPase from yeast (Mazhab-Jafari et al., 2016; Roh et al., 2018; Zhao et al., 2015), mammalian brain (Abbas et al., 2020; R. Wang et al., 2020), and cultured human cells (L. Wang et al., 2020), endogenous transiently-interacting proteins have not been characterized structurally. One reason for this absence of associated proteins in structures is that each three-dimensional (3D) map in cryoEM shows the average structure from the 2D particle images included in the dataset of images. Consequently, if a bound protein is found in only a small fraction of particle images, it will appear in the resulting 3D map with a lower density than stoichiometric components of the complex.

To identify low abundance complexes between V-ATPase and its binding partners, we subjected a preparation of the enzyme from porcine kidney tissue to an exhaustive 3D classification strategy designed to detect low-population structures. This procedure revealed a small population of V-ATPase complexes with super-stoichiometric occupancy of the C subunit, and a second small population of complexes with an additional density bound to the catalytic A_3B_3 subcomplex and one of the peripheral stalks. We tentatively identified this protein as the TLDc

domain containing protein mEAK7 using mass spectrometry and subsequently confirmed the interaction and determined a high-resolution structure of V-ATPase with recombinant mEAK7. mEAK7 has been proposed to activate the mechanistic target of rapamycin (mTOR) pathway but was not previously suggested to interact with V-ATPase (Mendonça et al., 2020; Nguyen et al., 2019, 2018). The structure shows that the TLDc domain and a C-terminal domain are critical for V-ATPase interaction. We also show that the yeast TLDc-containing protein Oxr1p binds yeast V-ATPase, suggesting that TLDc domains are conserved V-ATPase interacting motifs. The mEAK7 C-terminal domain is unique among TLDc-containing proteins and forms an α helix that binds to the central rotor of the V-ATPase, thereby crosslinking the stator and rotor parts of the enzyme. This crosslink would be expected to block rotation and ATP hydrolysis by the enzyme. Intriguingly, mEAK7 binding does not inhibit activity both *in vitro* and in cells, with ATP hydrolysis partially disrupting the interaction. This behavior suggests that mEAK7 interaction with V-ATPase is sensitive to activity of the enzyme, which may relate to mEAK7's previously proposed roles in cellular signaling.

Results and Discussion

Overall structure of the porcine kidney V-ATPase

In order to identify low-abundance complexes between V-ATPases and the proteins that bind to it in cells, we isolated intact V-ATPase from porcine kidney using a fragment of the bacterial effector protein SidK (Abbas et al., 2020) (Fig. 1A). Extracting the enzyme from membranes with the detergent glyco-diosgenin (GDN) retained subunit H in the complex, similar to extraction with other mild detergents (L. Wang et al., 2020; R. Wang et al., 2020). Multiple V-ATPase subunits have isoforms encoded by different genes that are expressed in a tissue-dependent manner and targeted to different intracellular compartments (Toei et al., 2010). Mass spectrometry identified the isoform composition of the porcine kidney V-ATPase preparation as subunits A, B1, C, D, E1, F, G1 and H in the V_1 region, and subunits a1, c, c″, d1, e2, RNAseK, ATP6AP1/Ac45, and ATP6AP2/PRR in the V_O region (Fig. 1A, Fig. S1, Tables S1 and S2). Notably, these subunit isoforms correspond to the ubiquitous lysosomal V-ATPase subunits and, other than subunit B1, do not include the kidney-specific isoforms C2, G3, a4, or d2 (Toei et al., 2010). While initially surprising, this finding is consistent with the kidney-specific isoforms being expressed primarily in α-intercalated cells, which comprise <4% of kidney cells (Park et al., 2018). Despite the presence of bound SidK, which inhibits V-ATPase by ~30% (Maxson et al., 2021; Zhao et al., 2017), the specific ATPase activity of the preparation was 2.9 ± 0.72 μmol ATP/min/mg (± s.d., n=6 independent assays from two separate enzyme preparations). The preparation is also well-coupled, showing 91% inhibition by bafilomycin.

CryoEM of the preparation, combined with 3D classification during image analysis, led to three structures of the complex in each of its three main rotational states (Zhao et al., 2015) at nominal resolutions of 3.7 to 4.1 Å (Fig. 1B, *left*, Fig. S2 and S3, Table S3). Focused refinement of these maps improved the resolution of the V_1 regions to 3.6 to 4.0 Å and the V_O regions to 3.7 to 5.8 Å (Fig. S2 and S3). Combined with the identities of subunit isoforms from mass spectrometry, the cryoEM maps allowed for construction of atomic models of the porcine kidney V-ATPase in the different rotational states (Fig. 1B*, right*, and 1C, Fig. S4). These atomic models were complete except for residues 8 to 82 of subunit G1 in peripheral stalk 1 and residues 10 to 115 of subunit E1 in peripheral stalk 2, which were modelled as poly-alanine, and residues 667 to 713 of

subunit a1, which could not be modelled. Overall, the models of the porcine kidney V-ATPase closely resembles previous mammalian V-ATPase structures (Abbas et al., 2020; L. Wang et al., 2020; R. Wang et al., 2020). Further focused classification of the V_1 regions revealed an additional sub-state where the subunit AB pair that is usually ADP-bound lacks nucleotide and has a slightly different conformation than the ADP-bound, occluded, and open AB pairs (Abbas et al., 2020) (Fig S2D). This low-abundance state may exist in the catalytic cycle immediately before ATP binds.

Some kidney V-ATPase complexes have an additional C subunit or mEAK7 bound

In order to search for endogenous sub-stoichiometric binding partners of V-ATPase, signal corresponding to the known parts of the complex was estimated from the atomic models and subtracted from images (Bai et al., 2015). 3D classification (Scheres et al., 2007) was then performed within masks adjacent to the complex that were designed to contain any density that is not part of the V-ATPase (Fig. S5). To facilitate this analysis, a dataset comprising 737,357 particle images, including protein with a variety of nucleotide analogues, was subjected to the procedure. 3D classification revealed two small populations of complexes, each with a different additional density bound to the V-ATPase (Fig. 1C). The first population comprised ~3% of the dataset and is found in all three of the main rotational states of the enzyme, with 1.2% in State 1, 1.2% in State 2, and 0.6% in State 3. The additional density bridges peripheral stalks 1 and 3 of the V_1 region of the enzyme, which are usually not connected (Fig. 1A and C, *middle column*). This density appears to correspond to an additional copy of subunit C (Fig. 1D), which typically bridges peripheral stalks 2 and 3 (Fig. 1B and D). The observation of a population of V-ATPase complexes with two copies of subunit C explains previous native mass spectrometry of rat brain V-ATPase that indicated the existence of complexes with two C subunits (Abbas et al., 2020). The significance of this variant of the structure is not clear, but it may correspond to V-ATPase complexes that misassemble due to the dynamic nature of the association of the V_1 and V_O regions.

The second additional density is found in ~1.6% of particle images and only appeared with the complex in rotational State 2 (Fig. 1C, *right column*). This density abuts subunit B, subunit A, and peripheral stalk 3. The shape of the density does not correspond to any of the known subunits of V-ATPase. It is not clear if the fraction of particle images with this additional density represents the true fraction of V-ATPase complexes in cells with this protein bound, or if the interaction is more common but is disrupted during purification of V-ATPase. The list of proteins identified by mass spectrometry of the preparation (Table S1) was inspected to identify candidate proteins that could explain the density. After excluding V-ATPase subunits, the most abundant ~50 kDa proteins based on iBAQ scores (intensity Based Absolute Quantification) were the α and β subunits of mitochondrial ATP synthase followed by mEAK7. Structures are known for both subunit α and β from ATP synthase (Abrahams et al., 1994) and they do not fit the unexplained density, excluding them as the bound protein in the low-resolution cryoEM map. In contrast, a homology model of mEAK7 could be fit in the density with high-fidelity (Fig. 1E), suggesting that this extra density could be due to mEAK7.

mEAK7 interacts with catalytic subunits and a peripheral stalk from V-ATPase

mEAK-7 is the mammalian homologue of *Caenorhabditis elegans* EAK-7 (enhancer-of-akt-1-7), which regulates dauer formation in nematodes (Alam et al., 2010; Lee et al., 2001; Lin et al.,

2001). Mutations in *C. elegans* EAK-7 promote diapause and longevity (Alam et al., 2010). In mammals, mEAK-7 has been proposed to activate an alternative mTOR pathway, thereby regulating S6K2 activation and 4E-BP1 repression (Nguyen et al., 2018). To test the hypothesis that the additional density seen in Figure 1E is indeed mEAK7, DNA sequence encoding the protein was cloned into a vector with an N-terminal 6×His tag, expressed heterologously in *Escherichia coli*, and purified to homogeneity. Purified mEAK7 was mixed with porcine V-ATPase at ~20× molar excess and cryoEM specimens were prepared and subjected to structure determination. Particle images were again sorted into classes corresponding to the three main rotational states of the enzyme. The map of rotational State 2 showed V-ATPase with mEAK7 bound (Fig. 2A, *left*, Fig. S6A and B, Table S4, S5). The resolution of the map allowed for construction of an atomic model of the complex (Fig. 2A, *right*, and Fig. 2B). This atomic model of mEAK7 could be overlaid with the map from the endogenous complex with high fidelity (Fig. S6C), confirming the identity of the additional endogenous binding protein shown in Figure 1E as mEAK7. mEAK7 contains an N-terminal myristoylated motif (Fig. 2C, *red arrow*), followed by a region resembling an EF-hand domain (Fig. 2C, *cyan*), a TLDc domain (Fig. 2C, *yellow, green,* and *orange*), and a C-terminal α helix that is separated from the rest of the protein by an extended linker region (Fig. 2C, *red*) (Finelli and Oliver, 2017). The N terminus of mEAK7 is poorly resolved in the map, suggesting that it is disordered in the detergent-solubilized protein.

mEAK7 binding to V-ATPase is mediated through conserved regions in its TLDc domain and C-terminal α helix (Fig. 2D). The C-terminal α helix binds subunit D from the central rotor of V-ATPase as well as a B1 subunit, mediated mainly by multiple hydrophobic interactions (Fig. 2E). This α helix is formed from sequence in the protein that was previously proposed to bind mTOR (Nguyen et al., 2018). The structure shows that this sequence is sequestered from the cytoplasm and could not interact with mTOR, at least when mEAK7 is bound to V-ATPase. Remarkably, even in a 3D class that showed rotational State 2 with mEAK7 resolved poorly, strong density for the C-terminal α helix remained, suggesting that it forms a specific and high-affinity interaction with the complex. Binding of mEAK7 to rotational State 2 causes numerous subtle conformational changes throughout the complex (Fig. S6D). The structure of the TLDc domain resembles previously-determined TLDc domain structures (Fig. S6E).

The TLDc domain binds V-ATPase through interactions with subunits E1, A, and B1 (Fig. 2F). Binding involving subunit E1 occurs through apparent stacking interactions between Tyr341 from mEAK7 and Glu29 from subunit E1, electrostatic interaction between Lys384 from mEAK7 and Asn39 from subunit E1, and hydrophobic interactions between Tyr367 from mEAK7 and Ile40 from subunit E1. Binding involving subunit A occurs through apparent ionic interactions between Thr354 and Gln317 from mEAK7 with backbone atoms from residues Arg553 and Thr557 from A subunit, respectively, and hydrophobic interactions between Pro316 from mEAK7 and Ala559 from subunit A. Residues Gly276 and His277 from TLDc domain of mEAK7 interact with backbone atoms from Phe481 and Pro482 of subunit B1 through hydrophobic. Together the TLDc domain and C-terminal α helix form a pincer-like grip around B1 (Fig. 2A).

The domain homologous to an EF-hand motif consists of seven α helices (Fig. 2C and Fig. S7A). EF-hand motifs can bind or release other proteins in response to calcium binding (Burgoyne and Haynes, 2012). However, inspection of the sequence of the apparent EF-hand motif in mEAK7

shows that it is missing key conserved acidic residues needed for calcium binding (Fig. S7B) and is poorly conserved compared to rest of mEAK7 (Fig. 2D). Further, titration of mEAK7 with calcium did not notably change its circular dichroism spectrum (Fig. S7C) and cryoEM in the presence of calcium or the calcium chelators EDTA and EGTA did not change the structure of the mEAK6:V-ATPase complex (Fig. S7D). Consequently, the apparent EF-hand-like motif in mEAK7 appears to be structural rather than calcium sensing.

TLDc domains are V-ATPase interacting modules

The structure of mEAK7 bound to V-ATPase reveals how TLDc domains can bind to V-ATPase. TLDc domain-containing proteins are widespread in biology (Fig. S8A) (Finelli and Oliver, 2017). OXR1 (Merkulova et al., 2015) and NCOA7 (Castroflorio et al., 2021) are known to interact with V-ATPase, with mutation of the latter causing neurological effects. The short TLDc-containing NCOA7-B isoform is induced by interferons and also interacts with V-ATPase, inhibiting endosome-mediated viral entry into cells (Doyle et al., 2018). Together with the current finding that mEAK7 binds V-ATPase, these interactions suggest that TLDc domains are conserved V-ATPase-binding motifs. To test this hypothesis, we used *E. coli* to express the yeast TLDc-containing protein Oxr1p (Finelli and Oliver, 2017), which has not previously been proposed to interact with V-ATPase. Purified recombinant Oxr1p was mixed with purified yeast V-ATPase (Benlekbir et al., 2012) at a ~2-fold excess, and the mixture was subjected to cryoEM (Fig. S8B). The resulting 3D map shows Oxr1p bound to the A and B subunits of the V_1 region, as well as subunits E and G of peripheral stalk 2. This structure supports the hypothesis that TLDc domains from different proteins mediate interaction with V-ATPase. The TLDc domain of Oxr1p binds yeast V-ATPase differently than mEAK7 binds mammalian V-ATPase, attaching to peripheral stalk 2 rather than peripheral stalk 3. This variability shows that the binding geometry of TLDc domains with V-ATPase can vary between TLDc domain-containing proteins. Consistent with this variability, crystal structures of TLDc domains from human NCOA7-B, zebrafish OXR2, and fruit fly TBC1D24 show that while the overall TLDc fold is the same as in mEAK7, there are insertions and deletions in the domains near the V-ATPase binding regions (Fig. S6E).

mEAK7 interaction with V-ATPase does not affect enzyme activity

mEAK7 crosslinks the rotor and stator parts of V-ATPase, with its C-terminal α helix interacting with subunit D from the rotor and the TLDc domain interacting with peripheral stalk 3 and an AB pair (Fig. 2A). This interaction would be expected to inhibit ATP hydrolysis and proton pumping by V-ATPase, similar to chemical crosslinks between the rotor and stator in other rotary ATPases (Srivastava et al., 2018). To assess how mEAK7 affects V-ATPases activity, we performed ATPase assays with V-ATPase in the presence of recombinant mEAK7 (Fig. 3A). To our surprise, a 100× molar excess of mEAK7 did not detectably inhibit ATPase activity. The excess of mEAK7 also did not affect bafilomycin sensitivity of the preparation, showing that the V_1 and V_O regions of the enzyme remained coupled in the presence of mEAK7.

Perturbation of V-ATPase activity in cells would also be expected to affect the pH of lysosomes and phagosomes, which rely on V-ATPase for acidification. It is possible that mEAK7 expression in cells modulates V-ATPase activity by influencing the assembly status of the V_1 region with the V_O region (Kane, 1995; Sumner et al., 1995), which could affect the steady state pH of lysosomes and phagosomes. To detect mEAK7-induced changes in V-ATPase activity in

cells, we cloned mEAK7 into a vector for overexpression in mammalian cells. Ectopic expression of mEAK7 with a C-terminal mCherry tag in HEK293T cells with lysosomes labelled with FITC-dextran (Canton and Grinstein, 2015) confirmed the lysosomal localization of the protein, as shown previously (Nguyen et al., 2018) (Fig. 3B). As the C-terminal mCherry tag could interfere with binding of mEAK7's C-terminal α helix to V-ATPase subunit D, subsequent experiments were performed with untagged mEAK7 co-transfected with PLCδ-PH-RFP, a PtdIns(4,5)P_2 biosensor that associated with the inner leaflet of the plasma membrane (Botelho et al., 2000; Lemmon et al., 1995) but not with lysosomes, to confirm successful transfection. Consistent with the *in vitro* ATPase assays, expression of this construct in HEK293T cells (Fig. 3C) and macrophage-like RAW 264.7 cells (Fig. 3D) did not lead to changes in the steady state lysosomal pH or phagosomal pH, respectively (Canton and Grinstein, 2015). Together, these experiments indicate that mEAK7 expression neither inhibits nor activates V-ATPase *in vitro* or in cells.

V-ATPase binding by mEAK depends on it C-terminal α helix and is ATP-sensitive

To understand the relative importance of the TLDc domain and C-terminal α helix from mEAK7 in V-ATPase binding, we prepared a construct of mEAK7 with the C-terminal α helix removed by truncation at residue Ser415. This construct was expressed heterologously in *E. coli*, purified to homogeneity, and mixed with V-ATPase at ~20× molar excess for structure determination by cryoEM. As described above, intact mEAK7 binds V-ATPase in rotational State 2 and is seen in all 3D classes corresponding to this state (Fig. 4A, *left*). While 3D classification identified a population comprising ~25% of particle images where the density for mEAK7's N-terminal domain and TLDc domain are weak and poorly resolved, suggesting that they are loosely attached via the TLDc domain, density for the C-terminal α helix of mEAK7 remains strong and well resolved even in this 3D class (Fig. 4A, *upper left*, *circled in orange*). In contrast, when the C-terminal α helix is truncated most V-ATPase complexes in rotational State 2 do not bind mEAK7 (Fig. 4A, *upper middle*). Only ~22% of particle images showed any density for the N-terminal domain and TLDc domain of mEAK7 when the C-terminal α helix was truncated, and even this density was weak and poorly resolved (Fig. 4A, *lower middle*). These experiments indicate that mEAK7's C-terminal α helix is important for the tight binding of V-ATPase by mEAK7.

The observation that mEAK7, which crosslinks the rotor and stator of V-ATPase in the structure, does not affect the enzyme's activity *in vitro* or in cells suggests that the crosslink is broken during rotary catalysis. To determine the effect of ATP hydrolysis on mEAK7 crosslinking of the rotor and the stator, V-ATPase was mixed with a ~20× molar excess of mEAK7, ATP was added to 10 mM and mixed, and cryoEM grids were frozen within 5 s. Given the concentration of V-ATPase (20 mg/mL) and the enzyme's specific ATPase activity (2.9 ± 0.72 μmol ATP/min/mg), these conditions ensure that the grids were frozen before the supply of ATP was consumed. With ATP is added, a population of particles appeared with mEAK7 entirely absent in rotational State 2 (Fig. 4A, *right*). In this state, even density for the C-terminal α helix is missing (Fig. 4A, *right*, *orange dotted circle*), which does not occur with intact mEAK7 without ATP. Thus, it appears that rotation of the rotor, driven by ATP hydrolysis, can result in the displacement of mEAK7 from V-ATPase and disruption of the cross-link between the enzyme's rotor and stator. Despite several biochemical experiments, we were unable to demonstrate that mEAK7 can be fully dissociated from V-ATPase by the addition of ATP to the complex, suggesting that it can remain

associated to V-ATPase, either by its TLDc domain or its C-terminal α helix, during ATP hydrolysis.

It was previously shown that V-ATPase activity, but not V-ATPase mediated acidification of lysosomes, is necessary for mTOR signaling (Zoncu et al., 2011). Further, the C-terminal α helix of mEAK7 was previously proposed to interact directly with mTOR (Nguyen et al., 2018), which could not occur when mEAK7 is attached to V-ATPase. The observed ATP-sensitive interaction of mEAK7 with V-ATPase could relate to its proposed roles: partial displacement of mEAK7 from V-ATPase during ATP hydrolysis by V-ATPase would allow one of the domains from mEAK7 to bind other proteins (Fig. 4B, Video 1). To detect mEAK7 binding interactions that could occur when the protein is fully or partially separated from V-ATPase, we prepared a construct with N-terminally 3×FLAG tagged mEAK7 and incubated it with both porcine kidney and brain lysate in presence of 1% CHAPS. We then purified the mEAK7 by affinity chromatography and identified enriched proteins by mass spectrometry (Fig. S9). As a control experiment, proteins from an identical purification in the absence of 3×FLAG-tagged mEAK7 were also identified. This experiment showed specific enrichment of numerous V-ATPase subunits, but no additional interacting proteins could be detected with confidence. It is possible that interaction of the C-terminal α helix from mEAK7 with other proteins relies on post-translational modifications, as this region of the protein was found to be phosphorylated at Ser440, 444 and 446 in multiple cellular contexts (Wilhelm et al., 2014). Phosphorylation of these residues would likely prevent the C-terminal domain from binding V-ATPase and could also serve as a mechanism for regulating mEAK7 binding to V-ATPase and other proteins. Alternatively, separation of mEAK7 from V-ATPase could expose new binding sites on V-ATPase for other interacting protein. Finally, it is possible that protein interactions with mEAK7 were missed due to their occurring at sub-stoichiometric levels, with low affinity, or in different cellular contexts.

In summary, we determined the structure of complete V-ATPase from porcine kidney. Exhaustive 3D classification identified a population of the complex with an additional C subunit and another population with mEAK7 bound. The high-resolution structure of V-ATPase with mEAK7 shows that the TLDc domain and C-terminal α helix are needed for V-ATPase binding and provide a blueprint for how TLDc domains in other proteins interact with V-ATPases. mEAK7 binding did not perturb V-ATPase activity *in vitro* or in cells, suggesting that either the TLDc domain or C-terminal α helix detaches from V-ATPase while the enzyme is active, a hypothesis supported by cryoEM of the complex frozen in the presence of ATP. How the labile binding of mEAK7 to V-ATPase relates to the *in vivo* activity of the protein remains unclear and warrants further study, but it is possible that mEAK7 could function as a sensor for V-ATPase activity. The structures presented here suggest that labile activity-sensitive interactions can occur between V-ATPase and other proteins, including those that contain TLDc domains.

Author contributions:
Y.Z.T. co-developed the protein purification strategy, purified protein, performed biochemical assays, and performed cryo-EM and image analysis, built atomic models. Y.M.A. co-developed the initial purification strategy. S.A.B. co-developed the initial V-ATPase purification strategy. D.W. identified subunit isoforms for V-ATPase in preparation with supervision from C.V.R. G.G.H. identified proteins that bound to recombinant mEAK7 with supervision form A.-C.G.

J.W. measured the effect of mEAK7 overexpression on lysosome and phagosome pH with supervision from S.G. J.L.R. conceived the project, and supervised and coordinated experiments. Y.Z.T. and J.L.R. wrote the manuscript and prepared the figures with input from the other authors.

Acknowledgements
We thank S. Benlekbir for assistance with cryo-EM data collection, Z.-Y. Lin for assistance with mass spectrometry sample preparation and analysis, G. Wasney and S. Popa assistance with circular dichroism, A. Kotecha and F.J.A. Koh for data collection for the V-ATPase sample with mEAK7 and calcium using the Glacios microscope with Falcon4 Selectris X, B. McDougall for providing porcine tissue, and members of the Rubinstein laboratory for discussions. This work was supported by the Canadian Institutes of Health Research (CIHR) Project Grant PJT166152 (J.L.R.), CIHR Foundation grants FDN-143202 (S.G.) and FDN-143301 (A.-C.G). The Canada Research Chairs program (J.L.R. and A.-C.G), Canadian Cancer Society Research Institute i2I grant 705938 (A.-C.G.), Wellcome Trust, grant 221795/Z/20/Z (C.V.R.), Canadian Institutes of Health Research Postdoctoral fellowship (Y.Z.T., Y.M.A.), Agency for Science, Technology and Research Singapore R-154-000-C62-133 (Y.Z.T.), National University of Singapore (NUS) Presidential Young Professorship (Y.Z.T.). Cryo-EM data was collected at the Toronto High-Resolution High-Throughput cryo-EM facility, supported by the Canada Foundation for Innovation and Ontario Research Fund. Some of the proteomics experiments were performed at the Network Biology Collaborative Centre at the Lunenfeld-Tanenbaum Research Institute, a facility supported by Canada Foundation for Innovation funding, by the Government of Ontario, and by Genome Canada and Ontario Genomics (OGI-139).

Conflict of Interests
The authors declare that they have no conflict of interest.

Data and materials availability
CryoEM maps have been deposited into the EMDB as EMD- XXXX. Models have been deposited into the PDB as XXXX.

Methods

Protein purification

Porcine kidneys were chilled to 4 °C in 1L of homogenization buffer (4 mM HEPES pH 7.4, 320 mM sucrose, 0.2 mM PMSF). All subsequent steps were performed at 4 °C. Each kidney was dissected to separate the softer cortex and medulla tissue from the more rigid pelvis tissue. The cortex and medulla tissue were blended with homogenization buffer for 1 min in a total volume of ~500 mL for four kidneys at high speed followed by a 10 s pause and an additional 1 min of blending. Cell debris was removed by centrifugation at 800 ×g for 20 min. The membrane fraction from cells was then collected by centrifugation at 25,000 ×g for 20 min and flash frozen and stored at -80 °C. To solubilize the V-ATPase, solubilization buffer (50 mM HEPES pH 7, 320 mM sucrose, 300 mM NaCl, 10% [v/v] glycerol, 5 mM EDTA, 5 mM aminocaproic acid, 5 mM para aminobenzamidine, 0.2 mM PMSF) was added to the membrane fraction at 8 mL/g and resuspended with a Dounce homogenizer. Approximately 6 g of membranes were used for each preparation. The detergent glycol diosgenin (GDN) was added to 1% (w/v) and incubated with gentle mixing overnight. Following solubilization, V-ATPase purification and assay was performed as described previously (Abbas et al., 2020) except with 0.025% (w/v) GDN as the detergent and gel filtration with a Superose 6 Increase 10/300 column (GE Healthcare) following affinity purification.

Recombinant mEAK7 from *Sus scrofa* (uniprot ID: A0A4X1T484) was synthesized in a pET28 vector with N-terminal 6×His tag (GenScript). ArcticExpress competent cells (Agilent) were transformed with the plasmid and plated onto Luria broth (LB) agar supplemented with 50 μg mL^{-1} kanamycin (Sigma) and grown overnight at 37 °C. A transformed colony was used to inoculate a starter culture containing 10 mL of 2xYT medium supplemented with 50 μg mL^{-1} kanamycin. The starter culture was grown overnight at 37 °C with shaking at 240 rpm, and 10 mL of this culture was used to inoculate 1 L of 2xTY medium supplemented with 50 μg mL^{-1} kanamycin. The culture was grown at 37 °C with shaking at 240 rpm to an OD of ~0.8, with the temperature then reduced to 7 °C and protein expression was induced overnight by addition of 1 mM isopropyl β-D-1-thiogalactopyranoside (IPTG) (Fisher). All further steps were performed at 4 °C. Cells were harvested by centrifugation at 4000 ×g for 15 min and the cell pellet was resuspended in phosphate buffered saline (PBS) and centrifuged again at 4000 ×g for 30 min. The cell pellet was then resuspended in lysis buffer (50 mM Tris-HCl pH 7.4, 300 mM NaCl, 0.2 mM PMSF) at ~8 mL/g of wet cell pellet. The resuspended cells were lysed by sonication (Q Sonica Q500) with 2 s on, 2 s off at 30 % amplitude for 10 min and cell debris was removed by centrifugation at 130,000 ×g for 45 min with a Type 70 Ti Rotor (Beckman Coulter). The supernatant was filtered through a 0.22 μm filter (Sigma) and loaded onto a HisTrap HP 5 mL column previously equilibrated with HisTrap buffer (50 mM Tris-HCl pH 7.4, 300 mM NaCl, 20 mM imidazole). The column was washed with 10 column volumes (CV) of HisTrap buffer followed by elution with 5 CV of HisTrap buffer with imidazole added to 300 mM. Eluted protein was concentrated with a 10 kDa MWCO concentrator (Amicon) to ~500 μL before two rounds of gel filtration, first with a Superose 6 Increase 10/300 column and then a Superdex 75 10/300 column. The purified protein was pooled, flash frozen, and stored at -80 °C for subsequent use.

Cryo-EM sample preparation, data collection, and image analysis
Purified V-ATPase was concentrated to ~20 mg/mL and 1.2 µL was applied onto the copper side of nanofabricated gold grids (Marr et al., 2014) in the environmental chamber of a Leica EM GP2 grid freezing device (>80% RH, 277 K). Grids were blotted on the copper side for 1 s before plunge freezing in liquid ethane. To freeze grids with V-ATPase and mEAK7, V-ATPase at 20 mg/mL was mixed with a ~20× molar excess of mEAK7 (~1 mg/mL) and incubated for 30 minutes on ice. For grids with V-ATPase, mEAK7, and ATP, V-ATPase was first incubated with mEAK7 on ice. ATP with $MgCl_2$ at 50 mM (0.4 µL) was applied on the grid, and immediately before plunge freezing, 1.6 µL of V-ATPase:mEAK7 mixture was added and mixed by pipetting for 2 s. This procedure results in a final concentration of 10 mM ATP and requires a total of 5 s from mixing to plunge freezing.

For the V-ATPase alone, cryoEM data was acquired at 300 kV with a Thermo Fisher Scientific Titan Krios G3 electron microscope and prototype Falcon 4 camera operating in electron counting mode. The calibrated pixel size was 1.02 Å/pixel and 5,455 movies, consisting of 29 exposure fractions each with a total exposure of 40 $e^-/Å^2$, were collected. For V-ATPase with recombinant mEAK7, mEAK7ΔCterm, mEAK7 plus ATP, and mEAK7 plus EDTA with EGTA, cryoEM data was acquired with the same electron microscope. However, for these datasets a lower magnification was used with a calibrated pixel size of 1.3225 Å/pixel, and 5,142, 2,013, 5,498, and 2,468 movies consisting of 29 exposure fractions each with total exposures of 36, 37, 44, and 41 $e^-/Å^2$, respectively, were collected. For the V-ATPase with mEAK7 and calcium, a Thermo Fisher Scientific Glacios electron microscope and Falcon 4 camera with Selectris X energy filter was used. The slit width was 10 eV, and aberration-free image shift (AFIS) was used during data collection. The calibrated pixel size was 0.895 Å/pixel and 3,209 movies with 1288 frames in EER mode (Guo et al., 2020) with a total exposure of 40 $e^-/Å^2$ were collected. All data was collected using the EPU data collection software and, except for the sample with calcium added, monitored using *cryoSPARC* Live (Punjani et al., 2017).

For V-ATPase alone, movies were aligned with UCSF MotionCor2 (Zheng et al., 2017) through *Relion* v3 (Scheres, 2012) and processed using *cryoSPARC* v3. CTF parameters were estimated in patches and template selection of particle images performed using the map of rat brain V-ATPase as the reference (Abbas et al., 2020). 2D classification was then performed to remove undesirable particle images. Multiple rounds of *ab initio* refinement were used to further clean the dataset and a consensus 3D map at 3.9 Å resolution from 133,337 particle images was calculated with non-uniform refinement (Punjani et al., 2020). This consensus set of particle images, with their corresponding orientation parameters, were transferred to *Relion* v3 for particle polishing (Zivanov et al., 2019) and transferred back into *cryoSPARC* for heterogenous refinement to separate the three rotational states and for CTF refinement. Non-uniform refinement was then done for each of the three rotational states. For the other datasets, a similar processing strategy was used. For EER data, movies were converted to TIF files containing 46 exposure fractions using *relion_convert_to_tiff*. Transfer of data between *Relion* and *cryoSPARC* was done with *pyem* (10.5281/zenodo.3576630).

Exhaustive focused classification
Exhaustive focused classification was done by adapting the *Relion* signal subtraction and focused classification strategy (Bai et al., 2015). The dataset of particle images, including datasets with

additional nucleotide, were classified into the three main rotational states of the enzyme. Next, a model of the enzyme was fitted into the map and used to create a mask for subtracting signal from the core V-ATPase complex from individual particles. A mask that surrounds the V-ATPase complex but extends ~20 Å from the surface of complex was then created to search for weakly-bound proteins. This search space was divided into four main regions: the V_1 region, the region above V_1, the region adjacent to subunit a, and the region surrounding ATP6AP1/Ac45. Focused classification was then performed using each of these four masks. Particle orientation parameters were not refined and a range of T values were tested, as outlined previously (Bai et al., 2015). Fifteen classes were used during classification. If a potential additional density was identified, a new and tighter mask around the region of interest was created to select the signal of interest.

Atomic model building

The atomic models from rat brain V-ATPase (Abbas et al., 2020), the H subunit from human V-ATPase (L. Wang et al., 2020), and an mEAK7 model predicted by Phyre2 (Kelley et al., 2015) were used to begin model building. Models were built manually in *Coot* (Emsley and Cowtan, 2004) and refined with iterative rounds of adjustment in *Coot*, *Rosetta relax* (Wang et al., 2016), and real space refinement with *Phenix* (Adams et al., 2010; Afonine et al., 2018). This process was continued until statistics calculated with *Molprobity* (Chen et al., 2010) ceased to improve. The final map and model were validated with *cryoSPARC*'s implementation of *blocres* (Cardone et al., 2013) to assess map local resolution, the *3DFSC* suite (Tan et al., 2017) to calculate directional resolution anisotropy, and the *SCF* program (Baldwin and Lyumkis, 2020) to calculate the sampling compensation factor, which quantifies how preferred particle orientations contribute to attenuation of the Fourier Shell Correlation (FSC). Map-to-model FSCs were calculated by converting the model to a map with the *molmap* function in *Chimera* at the Nyquist resolution. A mask was made from this map with *Relion* (after low-pass filtering to 8 Å, extending by one pixel, and applying a cosine-edge of three pixels), and was applied to the map. Map-to-model FSC was calculated with *proc3d* in *EMAN* (Ludtke et al., 1999).

Mass Spectrometry

Mass spectrometry analysis of the purified V-ATPase and isoform identification was performed as described previously (Abbas et al., 2020). To identify proteins that bind mEAK7 by mass spectrometry, purified mEAK7 with 3×FLAG tag was immobilized on M2 affinity gel matrix (2 mL) and washed with ten CVs of buffer (50 mM HEPES pH 7, 300 mM NaCl, 10% [v/v] glycerol) to remove unbound mEAK7. Membrane fractions (prepared in the same manner for protein purification) were incubated with 1% (w/v) CHAPS for 2 h and passed through the column, followed by ten CVs of wash buffer (300 mM NaCl, 50 mM HEPES pH 7, 10% [v/v] glycerol, 0.3% [w/v] CHAPS), and finally 3 CVs of wash buffer with 150 µg/ml 3×FLAG peptide to elute the mEAK7. The eluted protein was concentrated and prepared for mass spectrometry using S-Trap Micro spin columns (Protifi) according to manufacturer's instructions. Each sample (5 µL in 5 % formic acid) was loaded at 800 nL/min onto an equilibrated HPLC column and peptides were eluted over a 90 min gradient generated by a Eksigent ekspertTM nanoLC 425 (Eksigent) nano-pump and analysed on a TripleTOF 6600 instrument (SCIEX) operated in data-dependent acquisition (DDA) mode. The DDA method consisted of one 250 ms MS1 TOF survey scan from 400–1800 Da followed by ten 100 ms MS2 candidate ion scans from 100–1800 Da in high sensitivity mode. Only ions with a charge of 2+

to 5+ that exceeded a threshold of 300 cps were selected for MS2, and former precursors were excluded for 7 s after one occurrence. To minimize carryover between each sample, the analytical column was washed for 2 h by running an alternating sawtooth gradient from 35% acetonitrile with 0.1% formic acid to 80% acetonitrile with 0.1% formic acid at a flow rate of 1500 nL/min, holding each gradient concentration for 5 min. Analytical column and instrument performance were verified after each sample by loading 30 fmol bovine serum albumin (BSA) tryptic peptide standard with 60 fmol α-casein tryptic digest and running a short 30 min gradient. TOF MS mass calibration was performed on BSA reference ions before running the next sample to adjust for mass drift and verify peak intensity.

All raw (WIFF and WIFF.SCAN) files were saved in ProHits (Liu et al., 2016). mzXML files were generated from raw files using the ProteoWizard converter converter (v3.0.4468) and SCIEX converter (v1.3 beta), implemented within ProHits. The searched databases contained the pig (v88) or rat (v97) complement of the RefSeq protein database (including reversed sequences and common contaminants: 128008 and 134277 total sequences respectively). mzXML files were searched by Mascot (v2.3.02) and Comet (v2016.01 rev. 2) using the following parameters: up to two missed trypsin cleavage sites, methionine oxidation and asparagine/glutamine deamidation as variable modifications. The fragment mass tolerance was 0.15 Da and the mass window for the precursor was ±40 ppm with charges of 2+ to 4+ (both monoisotopic mass). Search engine results were analyzed using the Trans-Proteomic Pipeline (TPP v4.6 OCCUPY rev 3) via iProphet. Spectral count data were visualized using ProHits-viz (https://prohits-viz.org/) (Knight et al., 2017).

Localization of mEAK7 and ratiometric determinations of lysosomal and phagosomal pH
HEK293T cells were seeded on 18 mm glass coverslips at a density of 3×10^5 cells/mL and were transfected with FuGENE 6 (Promega) transfection reagent 24 h later. RAW264.7 cells were seeded on 18 mm glass coverslips at a density of 5×10^5 cells/mL and transfected 24 h later with FuGENE HD. Cells were transfected with 3 µL of FuGENE per 1 µg of total plasmid. Both cell types were imaged 18 to 24 h post-transfection.

To visualize lysosomal compartments, HEK293T cells transiently expressing mEAK7-mCherry were incubated with 250 µg/mL fluorescein isothiocyanate (FITC)-conjugated 10 kDa-dextran at the time of transfection and chased with complete medium 1 h prior to imaging. Coverslips with cells were mounted in a Chamlide magnetic chamber, incubated at 37 ºC in HBSS medium, and visualized with a Zeiss Axiovert 200M confocal microscope operated by Volocity v6.3 software. Images were acquired using a 63×/1.4 NA oil objective (Zeiss) with an additional 1.5× magnifying lens and processed using Volocity v6.3 and Adobe Illustrator.

HEK293T cells transiently transfected with unlabelled mEAK7 and PLC*δ*-PH-RFP (to allow identification of transfected cells) were incubated with 250 µg/mL FITC-conjugated 10 kDa-dextran at the time of transfection and chased with complete medium 1 h prior to imaging to visualize lysosomal compartments. RAW264.7 cells co-transfected with unlabelled mEAK7 and PLC*δ*-PH-RFP were incubated with FITC-conjugated zymosan particles, which were taken up into phagosomes, 1 h prior to imaging and were chased with complete medium 30 min prior to imaging to wash away unbound particles. Steady-state lysosomal and phagosomal pH were determined by exciting FITC labelled lysosome/phagosomes at 481 ± 15 nm and 436 ± 20 nm,

respectively, and collecting emitted light at 520 ± 35 nm. The pH-dependent fluorescence intensity of FITC when excited at ~490 nm was used as described below to determine the steady-state pH of lysosomes. The much less pH-sensitive fluorescence intensity of FITC when excited at ~440 nm was used to control for photobleaching during image acquisition. Multiple fields of cells were imaged for each condition, and the data processed was with Volocity v6.3. To convert fluorescence ratios to pH values, cells were sequentially subjected to isotonic K^+ solutions (143 mM KCl, 5 mM glucose, 1 mM $MgCl_2$, 1 mM $CaCl_2$) at different pH values (pH 4.5 solution buffered with 20 mM acetic acid, pH 5.5, 6.5, and 7.5 solutions buffered with 20 mM MES), containing 10 μM nigericin and 5 μM monensin. Cells were imaged 5 min after the addition of each solution to obtain the 490 nm/440 nm fluorescence ratio corresponding to each pH standard. A calibration curve was prepared from a least squares fit of mean background-subtracted fluorescence ratios as a function of pH.

References

Abbas YM, Wu D, Bueler SA, Robinson C V, Rubinstein JL. 2020. Structure of V-ATPase from the mammalian brain. *Science (80-)* **1**:1240–1246.

Abrahams JP, Leslie AG, Lutter R, Walker JE. 1994. Structure at 2.8 A resolution of F1-ATPase from bovine heart mitochondria. *Nature* **370**:621–628. doi:10.1038/370621a0

Adams PD, Afonine P V., Bunkóczi G, Chen VB, Davis IW, Echols N, Headd JJ, Hung LW, Kapral GJ, Grosse-Kunstleve RW, McCoy AJ, Moriarty NW, Oeffner R, Read RJ, Richardson DC, Richardson JS, Terwilliger TC, Zwart PH. 2010. PHENIX: A comprehensive Python-based system for macromolecular structure solution. *Acta Cryst* **D66**:213–221. doi:10.1107/S0907444909052925

Afonine P V., Poon BK, Read RJ, Sobolev O V., Terwilliger TC, Urzhumtsev A, Adamsa PD. 2018. Real-space refinement in PHENIX for cryo-EM and crystallography research papers. *Acta Cryst* **D74**:531–544. doi:10.1107/S2059798318006551

Alam H, Williams TW, Dumas KJ, Guo C, Yoshina S, Mitani S, Hu PJ. 2010. EAK-7 controls development and life span by regulating nuclear DAF-16/FoxO activity. *Cell Metab* **12**:30–41. doi:10.1016/j.cmet.2010.05.004

Bai XC, Rajendra E, Yang G, Shi Y, Scheres SHW. 2015. Sampling the conformational space of the catalytic subunit of human g-secretase. *Elife* **4**:1–19. doi:10.7554/eLife.11182

Baldwin PR, Lyumkis D. 2020. Non-uniformity of projection distributions attenuates resolution in. *Prog Biophys Mol Biol* **150**:160–183. doi:10.1016/j.pbiomolbio.2019.09.002

Benlekbir S, Bueler SA, Rubinstein JL. 2012. Structure of the vacuolar-type ATPase from Saccharomyces cerevisiae at 11-Å resolution. *Nat Struct Mol Biol* **19**:1356–62. doi:10.1038/nsmb.2422

Botelho RJ, Teruel M, Dierckman R, Anderson R, Wells A, York JD, Meyer T, Grinstein S. 2000. Localized Biphasic Changes in Phosphatidylinositol-4 , 5-Bisphosphate at Sites of Phagocytosis. *J Cell Biol* **151**:1353–1367.

Burgoyne RD, Haynes LP. 2012. Understanding the physiological roles of the neuronal calcium sensor proteins. *Mol Brain* **5**. doi:10.1186/1756-6606-5-2

Canton J, Grinstein S. 2015. Measuring lysosomal pH by fluorescence microscopy. *Methods Cell Biol* **126**:85–99. doi:10.1016/bs.mcb.2014.10.021

Cardone G, Heymann JB, Steven AC. 2013. One number does not fit all: Mapping local variations in resolution in cryo-EM reconstructions. *J Struct Biol* **184**:226–236.

doi:10.1016/j.jsb.2013.08.002
Castroflorio E, Hoed J Den, Svistunova D, Finelli MJ, Cebrian A. 2021. The Ncoa7 locus regulates V - ATPase formation and function , neurodevelopment and behaviour. *Cell Mol Life Sci*. doi:10.1007/s00018-020-03721-6
Chen VB, Arendall WB, Headd JJ, Keedy DA, Immormino RM, Kapral GJ, Murray LW, Richardson JS, Richardson DC. 2010. MolProbity: all-atom structure validation for macromolecular crystallography. *Acta Cryst* **D66**:12–21. doi:10.1107/S0907444909042073
Cruciat CM, Ohkawara B, Acebron SP, Karaulanov E, Reinhard C, Ingelfinger D, Boutros M, Niehrs C. 2010. Requirement of prorenin receptor and vacuolar H+-ATPase-mediated acidification for Wnt signaling. *Science (80-)* **327**:459–463. doi:327/5964/459 [pii]10.1126/science.1179802
Doyle T, Moncorgé O, Bonaventure B, Pollpeter D, Lussignol M, Tauziet M, Apolonia L, Catanese M, Goujon C, Malim MH. 2018. The interferon-inducible isoform of NCOA7 inhibits endosome-mediated viral entry. *Nat Microbiol* **3**:1369–1376. doi:10.1038/s41564-018-0273-9
Eaton AF, Merkulova M, Brown D. 2020. The H + ATPase (V-ATPase): from proton pump to signaling complex in health and disease.
Emsley P, Cowtan K. 2004. Coot: Model-building tools for molecular graphics. *Acta Cryst* **D60**:2126–2132. doi:10.1107/S0907444904019158
Finelli MJ, Oliver PL. 2017. TLDc proteins: new players in the oxidative stress response and neurological disease. *Mamm Genome* **28**:395–406. doi:10.1007/s00335-017-9706-7
Finelli MJ, Sanchez-Pulido L, Liu KX, Davies KE, Oliver PL. 2016. The evolutionarily conserved Tre2/Bub2/Cdc16 (TBC), lysin motif (LysM), domain catalytic (TLDc) domain is neuroprotective against oxidative stress. *J Biol Chem* **291**:2751–2763. doi:10.1074/jbc.M115.685222
Forgac M. 2007. Vacuolar ATPases: rotary proton pumps in physiology and pathophysiology. *Nat Rev Mol Cell Biol* **8**:917–929. doi:10.1038/nrm2272
Guo H, Franken E, Deng Y, Benlekbir S, Singla G, Janssen B, Yu L, Ripstein ZA, Tan YZ, John L. 2020. Electron-event representation data enable efficient cryoEM file storage with full preservation of spatial and temporal resolution. *IUCrJ* **7**:860–869.
Kane PM. 1995. Disassembly and reassembly of the yeast vacuolar H(+)-ATPase in vivo. *J Biol Chem* **270**:17025–17032.
Kelley LA, Mezulis S, Yates CM, Wass MN, Sternberg MJE. 2015. The Phyre2 web portal for protein modeling, prediction and analysis. *Nat Protoc 2015 106* **10**:845–858. doi:10.1038/nprot.2015.053
Knight JDR, Choi H, Gupta GD, Pelletier L, Raught B, Nesvizhskii AI, Gingras A. 2017. ProHits-viz : a suite of web tools for visualizing interaction proteomics data PIQED : automated identification and quantification of protein modifications from DIA-MS data. *Nat Methods* **14**:645–646.
Lee BS, Gluck SL, Holliday LS. 1999. Interaction between Vacuolar H ⁄. -ATPase and Microfilaments during Osteoclast Activation * the resorption bay at the osteoclast attachment site on. *J Biol Chem* **274**:29164–29171. doi:10.1074/jbc.274.41.29164
Lee RY, Hench J, Ruvkun G. 2001. Regulation of C. elegans DAF-16 and its human ortholog FKHRL1 by the daf-2 insulin-like signaling pathway. *Curr Biol* **11**:1950–1957. doi:10.1016/S0960-9822(01)00595-4
Lemmon MA, Fergusonti KM, O'Brient R, Sigler PB, Schlessinger J. 1995. Specific and high-

affinity binding of inositol phosphates to an isolated pleckstrin homology domain. *Proc Natl Acad Sci U S A* **92**:10472–10476.
Lin K, Hsin H, Libina N, Kenyon C. 2001. Regulation of the Caenorhabditis elegans longevity protein DAF-16 by insulin/IGF-1 and germline signaling. *Nat Genet* **28**:139–145.
Liu G, Knight JDR, Liu G, Knight JDR, Zhang JP, Tsou C-C, Wang J, Lambert J, Larsen B, Tyers M, Raught B, Bandeira N, Nesvizhskii AI, Choi H, Gingras A. 2016. Data Independent Acquisition analysis in ProHits 4 . 0. *J Proteomics* **149**:64–68. doi:10.1016/j.jprot.2016.04.042
Lu M, Holliday LS, Zhang L, Dunn WA, Gluck SL. 2001. Interaction between aldolase and vacuolar H+-ATPase. Evidence for direct coupling of glycolysis to the ATP-hydrolyzing proton pump. *J Biol Chem* **276**:30407–30413. doi:10.1074/jbc.M008768200
Ludtke SJ, Baldwin PR, Chiu W. 1999. EMAN: semiautomated software for high-resolution single-particle reconstructions. *J Struct Biol* **128**:82–97. doi:10.1006/jsbi.1999.4174S1047-8477(99)94174-6 [pii]
Marr CR, Benlekbir S, Rubinstein JL. 2014. Fabrication of carbon films with approximately 500 nm holes for cryo-EM with a direct detector device. *J Struct Biol* **185**:42–47. doi:10.1016/j.jsb.2013.11.002
Maxson ME, Abbas YM, Wu JZ, Grinstein S, Rubinstein JL. 2021. Detection and quantification of the vacuolar H+-ATPase using the Legionella effector protein SidK. *bioRxiv* **10.1101/20**.
Mazhab-Jafari MT, Rohou A, Schmidt C, Bueler SA, Benlekbir S, Robinson C V., Rubinstein JL. 2016. Atomic model for the membrane-embedded VO motor of a eukaryotic V-ATPase. *Nature* **539**:118–122.
Mendonça DB, Nguyen JT, Haidar F, Fox AL, Ray C, Amatullah H, Liu F, Kim JK, Krebsbach PH. 2020. MicroRNA-1911-3p targets mEAK-7 to suppress mTOR signaling in human lung cancer cells. *Heliyon* **6**:e05734. doi:10.1016/J.HELIYON.2020.E05734
Merkulova M, Paunescu TG, Azroyan A, Marshansky V, Breton S, Brown D. 2015. Mapping the H+ (V)-ATPase interactome: Identification of proteins involved in trafficking, folding, assembly and phosphorylation. *Sci Rep* **5**:1–15. doi:10.1038/srep14827
Nguyen JT, Haidar FS, Fox AL, Ray C, Mendonça DB, Kim JK, Krebsbach PH. 2019. mEAK-7 Forms an Alternative mTOR Complex with DNA-PKcs in Human Cancer. *iScience* **17**:190–207. doi:10.1016/j.isci.2019.06.029
Nguyen JT, Ray C, Fox AL, Mendonça DB, Kim JK, Krebsbach PH. 2018. Mammalian EAK-7 activates alternative mTOR signaling to regulate cell proliferation and migration. *Sci Adv* **4**:1–16. doi:10.1126/sciadv.aao5838
Park J, Shrestha R, Qiu C, Kondo A, Huang S, Werth M, Li M, Barasch J, Suszták K. 2018. Single-cell transcriptomics of the mouse kidney reveals potential cellular targets of kidney disease. *Science (80-)* **360**:758–763. doi:10.1126/science.aar2131
Parra KJ, Keenan KL, Kane PM. 2000. The H subunit (VMA13p) of the yeast V-ATPase inhibits the ATPase activity of cytosolic V1 complexes. *J Biol Chem* **275**:21761–21767. doi:10.1074/jbc.M002305200
Punjani A. 2020. Algorithmic Advances in Single Particle Cryo-EM Data Processing Using CryoSPARC. *Microsc Microanal* **26**:2322–2323. doi:10.1017/s1431927620021194
Punjani A, Rubinstein JL, Fleet DJ, Brubaker MA. 2017. cryoSPARC: Algorithms for rapid unsupervised cryo-EM structure determination. *Nat Methods* **14**:290–296. doi:10.1038/nmeth.4169
Punjani A, Zhang H, Fleet DJ. 2020. Non-uniform refinement: adaptive regularization improves

single-particle cryo-EM reconstruction. *Nat Methods* **17**:1214–1221. doi:10.1038/s41592-020-00990-8

Roh S-H, Stam NJ, Hryc CF, Couoh-Cardel S, Pintilie G, Chiu W, Wilkens S. 2018. The 3.5-Å CryoEM Structure of Nanodisc-Reconstituted Yeast Vacuolar ATPase V o Proton Channel. *Mol Cell* **69**:993–1004. doi:10.1016/j.molcel.2018.02.006

Scheres SHW. 2012. RELION: implementation of a Bayesian approach to cryo-EM structure determination. *J Struct Biol* **180**:519–530. doi:10.1016/j.jsb.2012.09.006

Scheres SHW, Gao H, Valle M, Herman GT, Eggermont PPB, Frank J, Carazo J-M. 2007. Disentangling conformational states of macromolecules in 3D-EM through likelihood optimization. *Nat Methods* **4**:27–29. doi:10.1038/nmeth992

Srivastava AP, Luo M, Zhou W, Symersky J, Bai D, Chambers MG, Faraldo-Gómez JD, Liao M, Mueller DM. 2018. High-resolution cryo-EM analysis of the yeast ATP synthase in a lipid membrane. *Science* **9699**:eaas9699. doi:10.1126/science.aas9699

Sumner JP, Dow JA, Earley FG, Klein U, Jager D, Wieczorek H. 1995. Regulation of plasma membrane V-ATPase activity by dissociation of peripheral subunits. *J Biol Chem* **270**:5649–5653.

Tabke K, Albertmelcher A, Vitavska O, Huss M, Schmitz H-P, Wieczorek H. 2014. Reversible disassembly of the yeast V-ATPase revisited under *in vivo* conditions. *Biochem J* **462**:185–197. doi:10.1042/BJ20131293

Tan YZ, Baldwin PR, Davis JH, Williamson JR, Potter CS, Carragher B, Lyumkis D. 2017. Addressing preferred specimen orientation in through tilting. *Nat Methods* **14**:793–796. doi:10.1038/nmeth.4347

Toei M, Saum R, Forgac M. 2010. Regulation and isoform function of the V-ATPases. *Biochemistry* **49**:4715–4723. doi:10.1021/bi100397s

Vaccari T, Duchi S, Cortese K, Tacchetti C, Bilder D. 2010. The vacuolar ATPase is required for physiological as well as pathological activation of the Notch receptor. *Development* **137**:1825–1832. doi:10.1242/dev.045484

Vasanthakumar T, Rubinstein JL. 2020. Structure and Roles of V-type ATPases. *Trends Biochem Sci* **45**. doi:10.1016/j.tibs.2019.12.007

Wang L, Wu D, Robinson C V, Wu H, Fu T. 2020. Structures of a Complete Human V-ATPase Reveal Mechanisms of Its Assembly. *Mol Cell* **80**:1–11. doi:10.1016/j.molcel.2020.09.029

Wang R, Long T, Hassan A, Wang J, Sun Y, Xie XS, Li X. 2020. Cryo-EM structures of intact V-ATPase from bovine brain. *Nat Commun* **11**:1–9. doi:10.1038/s41467-020-17762-9

Wang RY, Song Y, Barad BA, Cheng Y, Fraser JS, Dimaio F. 2016. Automated structure refinement of macromolecular assemblies from cryo-EM maps using Rosetta. *Elife* **5**:e17219. doi:10.7554/eLife.17219

Wilhelm M, Schlegl J, Hahne H, Gholami AM, Lieberenz M, Savitski MM, Ziegler E, Butzmann L, Gessulat S, Marx H, Mathieson T, Lemeer S, Schnatbaum K, Reimer U, Wenschuh H, Mollenhauer M, Slotta-Huspenina J, Boese J-H, Bantscheff M, Gerstmair A, Faerber F, Kuster B. 2014. Mass-spectrometry-based draft of the human proteome. *Nat 2014 5097502* **509**:582–587. doi:10.1038/nature13319

Yan Y, Denef N, Schüpbach T. 2009. The Vacuolar Proton Pump, V-ATPase, Is Required for Notch Signaling and Endosomal Trafficking in Drosophila. *Dev Cell* **17**:387–402. doi:10.1016/j.devcel.2009.07.001

Zhao J, Benlekbir S, Rubinstein JL. 2015. Electron cryomicroscopy observation of rotational states in a eukaryotic V-ATPase. *Nature* **521**:241–245. doi:10.1038/nature14365

Zhao J, Beyrakhova K, Liu Y, Alvarez CP, Bueler SA, Xu L, Xu C, Boniecki MT, Kanelis V, Luo Z-Q, Cygler M, Rubinstein JL. 2017. Molecular basis for the binding and modulation of V-ATPase by a bacterial effector protein. *PLoS Pathog* **13**:e1006394. doi:10.1371/journal.ppat.1006394

Zheng SQ, Palovcak E, Armache J-P, Verba KA, Cheng Y, Agard DA. 2017. MotionCor2 : anisotropic correction of beam-induced motion for improved cryo-electron microscopy. *Nat Methods* **14**:331–332. doi:10.1038/nmeth.4193

Zivanov J, Nakane T, Scheres SHW. 2019. A Bayesian approach to beam-induced motion correction in cryo-EM single-particle analysis. *IUCrJ* **6**:5–17. doi:10.1107/S205225251801463X

Zoncu R, Bar-Peled L, Efeyan A, Wang S, Sancak Y, Sabatini DM. 2011. mTORC1 senses lysosomal amino acids through an inside-out mechanism that requires the vacuolar H-ATPase. *Science (80-)* **334**:678–683. doi:334/6056/678 [pii]10.1126/science.1207056

Figures

Figure 1. Structure of porcine kidney V-ATPase. A, SDS-PAGE gel showing subunit isoforms identified by mass spectrometry. **B,** CryoEM map (*left*) and atomic model (*right*) of V-ATPase from porcine kidney. **C,** Additional densities (*green*) bound to the V-ATPase. **D,** Fitting of an atomic model for subunit C into one of the additional densities. **E,** Fitting of a homology model for mEAK7 into the other additional density.

Figure 2. Structure of mEAK7 bound to V-ATPase crosslink's the enzyme's rotor and stator. A, CryoEM map (l*eft*) and atomic model (*right*) for recombinant mEAK7 bound to V-ATPase. **B,** Examples of model in map fit for mEAK7. **C,** Domain structure of mEAK7. **D,** Sequence conservation in mEAK7. The myristoylation motif in mEAK7 is indicated (*red arrow*). **E,** Interactions between the C-terminal α helix of mEAK7 and the rotor of V-ATPase. **F,** Interactions between the TLDc domain of mEAK7 and subunits from the stator of V-ATPase.

Figure 3. mEAK7 binding does not affect V-ATPase activity. A, Recombinant mEAK7 does not alter the ATPase activity or bafilomycin sensitivity of purified V-ATPase in vitro. **B,** mEAK7-mCherry localizes to lysosomes in HEK293T cells, which were labelled with fluorescein isothiocyanate (FITC)-conjugated 10 kDa-dextran. Scale bar, 10 µm. Overexpression of unlabeled mEAK7 does not alter the steady state pH of lysosomes in HEK293T cells (**C**) or phagosomes in RAW 264.7 cells (**D**).

Figure 4. C-terminal truncation and ATP hydrolysis suppress mEAK7 binding to V-ATPase. A, Intact mEAK7 in the absence of ATP (*left*) binds V-ATPase in rotational State 2, with its C-terminal α helix well-resolved in all 3D classes (*dashed orange ellipse*). Truncation of the C-terminal α helix results in 3D classes lacking bound mEAK7 *(center*). The addition of ATP to mEAK7 and V-ATPase (*right*) results in a 3D class lacking density for the TLDc domain of mEAK7 and its C-terminal α helix (*dashed orange ellipse*). **B,** ATP-hydrolysis induced disruption of the association between mEAK7 and V-ATPase could enable alternative functions in the cell.

Supplementary Figure 1. Mass spectrometry identification of subunit isoforms. A, Gel regions subjected to mass spectrometry. **B,** Subunit isoforms identified in each gel region. The colour density represents the normalized $\log_{10}$(iBAQ score). **C,** Approximate abundance of different subunit isoforms (iBAQ score).

Supplementary Figure 2. CryoEM workflow. A, Example micrograph. **B,** Example class average images. **C,** Workflow used to identify different conformations of V-ATPase. **D,** Focused refinement scheme used to produe high-resolution maps.

Supplementary Figure 3. CryoEM map validation. Fourier Shell Correlation curves following a gold-standard refinement and correction for masking, and orientation distribution plots, for rotational State 1A (**A**), State 1B (**B**), State 2A (**C**), State 2B (**D**), State 3A (**E**), and State 3B (**F**).

Supplementary Figure 4. Examples of model-in-map fit. Examples are shown from each of the different V-ATPase subunit types. Residue numbers shown are indicated in brackets.

Supplementary Figure 5. Exhaustive focused classification strategy for finding sub-stoichiometric proteins bound to V-ATPase. The process is show for rotational State 1 as an example, but was applied to all rotational states.

Supplementary Figure 6. mEAK7 binding to V-ATPase. A, Fourier shell correlation curve following a gold-standard refinement and correction for masking for the map of V-ATPase bound to mEAK7. **B,** Local resolution for mEAK7 in the cryoEM map of mEAK7 bound to V-ATPase. **C,** Comparison of the map for endogenous mEAK7 (*grey surface*) and atomic model for recombinant mEAK7 (*cyan ribbons*) bound to V-ATPase shows that the two structures are equivalent. **D,** Conformational changes to V-ATPase upon mEAK7 binding. **E,** Comparison of known structures of TLDc domains (left) and multiple sequence alignment (*right*) shows numerous insertions (numbered with Roman numerals for each structure).

Supplementary Figure 7. The EF-hand-like domain in mEAK7 does not bind calcium. A, Structural comparison of mEAK7 and the EF-hand-like domain in fruit fly Frq2. The three calcium binding sites are numbered with roman numerals. **B,** Sequence comparison of mEAK7 and the NCS-I domain in fruit fly Frq2, with red dots showing the residues in Frq2 that are involved in calcium binding and Roman numerals corresponding to the three calcium binding sites indicated in (A). Note that these residues are not well conserved in mEAK7. **C,** Circular dichroism spectroscopy of mEAK7 with varying concentrations of calcium. **D,** Experimental CryoEM maps (*grey surfaces*) for mEAK7 bound to V-ATPase with the chelators EGTA and EDTA (*left*), no chelator and no calcium (*middle*), and 20 mM calcium (*right*). The atomic model for mEAK7 (*cyan ribbons*) in the absence of chelator or calcium is shown fitted into each map.

Supplementary Figure 8. TLDc domains are V-ATPase binding domain. A, Comparison of domain arrangement in proteins that include TLDc domains. **B,** Structure of the *S. cerevisiae* protein Oxr1p bound to *S. cerevisiae* V-ATPase.

Supplementary Figure 9. Mass spectrometry identification of proteins that bind mEAK7. Proteins that bind recombinant 3×FLAG-mEAK7 upon incubation with kidney (**A**) and brain (**B**) lysate were identified and quantified approximately by the number of peptides found for each protein (*x-axis in each plot*). In a control experiment, proteins were quantified with an equivalent experiment that excluded 3×FLAG-mEAK7 (*y-axis in each plot*).

Supplementary Table 1. Proteins identified by mass spectrometry from each gel region in purified porcine kidney V-ATPase.

Supplementary Table 2. Mass spectrometry comparison of isoform content for different V-ATPase subunits.

Video 1. Illustration of mEAK7 binding and unbinding V-ATPase.

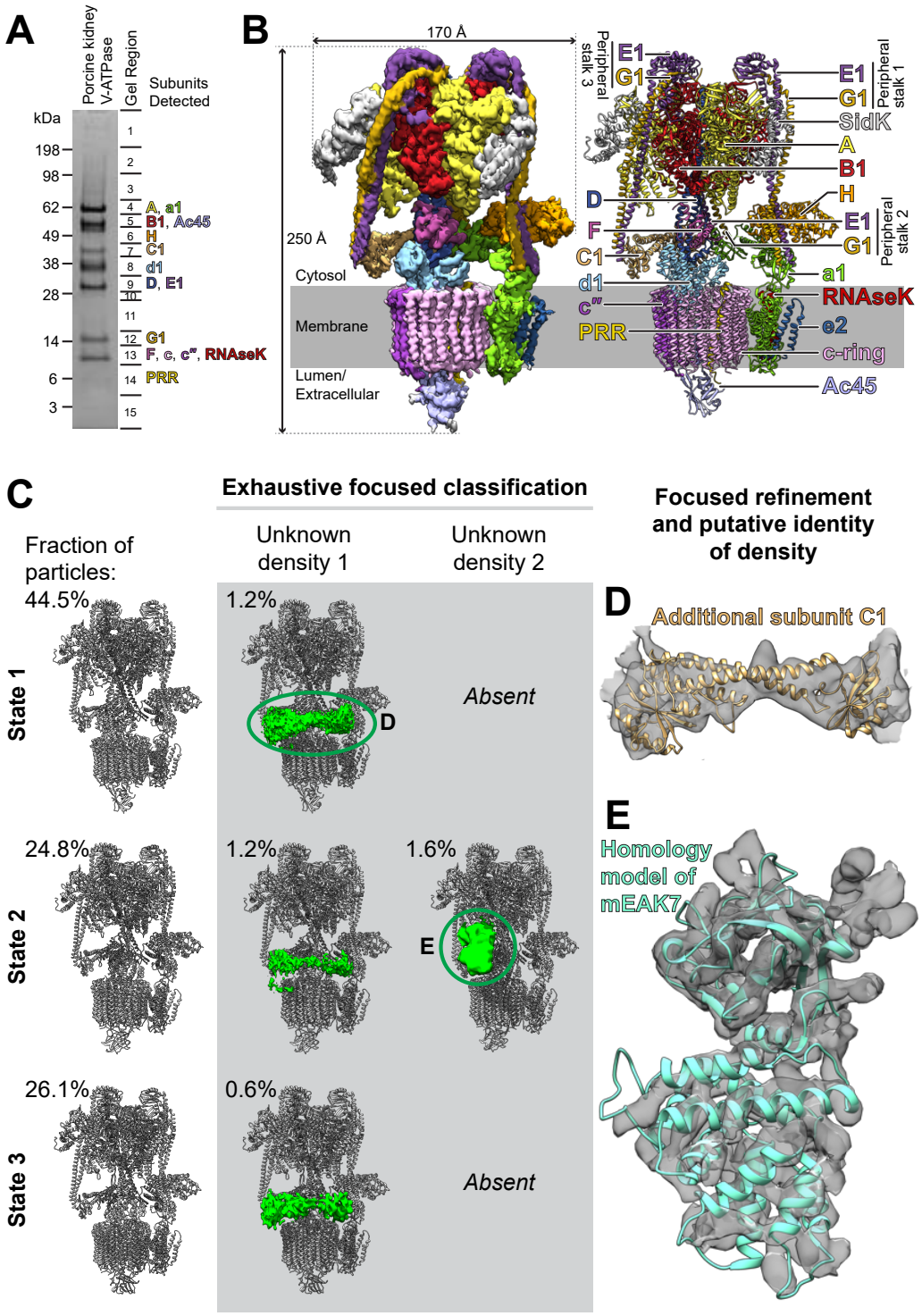
A
Porcine kidney V-ATPase
Gel Region
Subunits Detected
kDa
198
98
62
49
38
28
14
6
3
1
2
3
4
5
6
7
8
9
10
11
12
13
14
15
A, a1
B1, Ac45
H
C1
d1
D, E1
G1
F, c, c'', RNAseK
PRR
B
170 Å
250 Å
Cytosol
Membrane
Lumen/ Extracellular
Peripheral stalk 3
E1
G1
D
F
C1
d1
c''
PRR
Peripheral stalk 1
E1
G1
SidK
A
B1
H
Peripheral stalk 2
E1
G1
a1
RNAseK
e2
c-ring
Ac45
C
Exhaustive focused classification
Fraction of particles:
Unknown density 1
Unknown density 2
Focused refinement and putative identity of density
State 1
44.5%
1.2%
D
Absent
State 2
24.8%
1.2%
1.6%
E
State 3
26.1%
0.6%
Absent
D
Additional subunit C1
E
Homology model of mEAK7

Figure 1

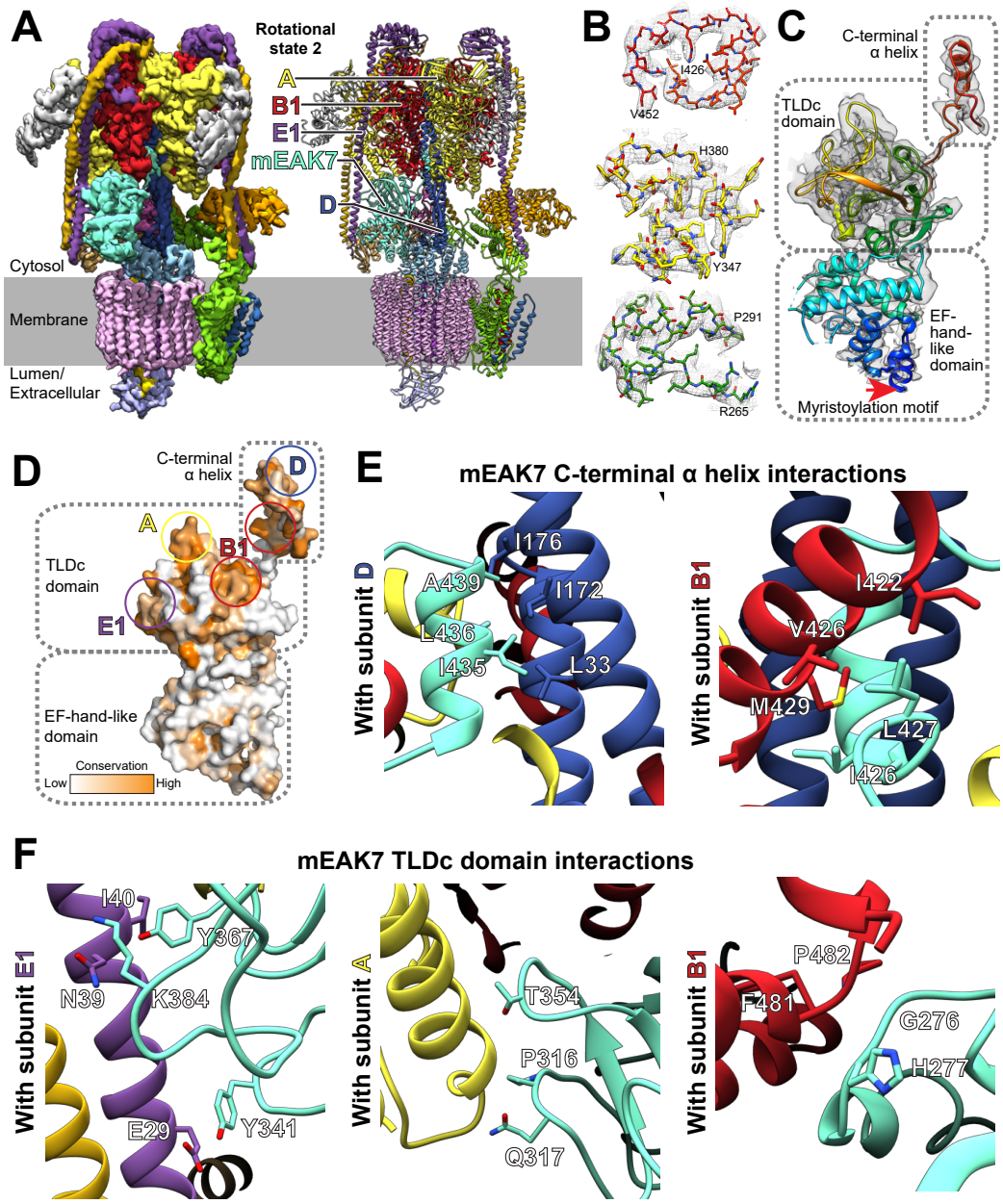
A
Rotational state 2
A
B1
E1
mEAK7
D
Cytosol
Membrane
Lumen/ Extracellular
B
I426
V452
H380
Y347
P291
R265
C
C-terminal α helix
TLDc domain
EF-hand-like domain
Myristoylation motif
D
C-terminal α helix
D
A
B1
TLDc domain
E1
EF-hand-like domain
Conservation
Low
High
E
mEAK7 C-terminal α helix interactions
With subunit D
I176
A439
I172
L436
I435
L33
With subunit B1
I422
V426
M429
L427
I426
F
mEAK7 TLDc domain interactions
With subunit E1
I40
Y367
N39
K384
E29
Y341
With subunit A
T354
P316
Q317
With subunit B1
P482
F481
G276
H277

Figure 2

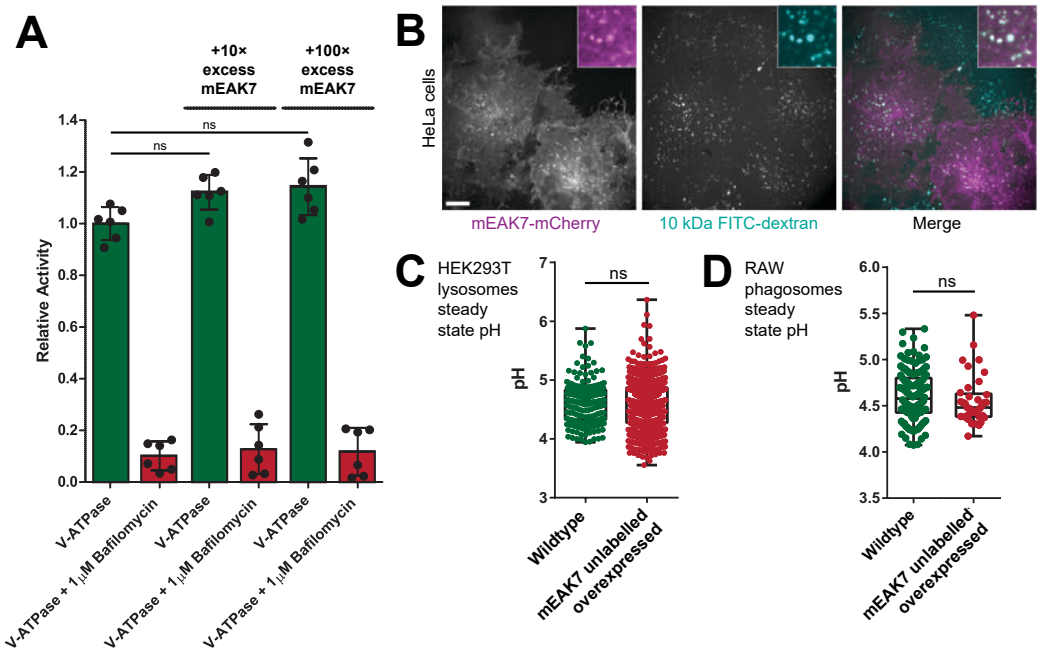
A
+10× excess mEAK7
+100× excess mEAK7
ns
ns
Relative Activity
1.4
1.2
1.0
0.8
0.6
0.4
0.2
0.0
V-ATPase
V-ATPase + 1 μM Bafilomycin
V-ATPase
V-ATPase + 1 μM Bafilomycin
V-ATPase
V-ATPase + 1 μM Bafilomycin
B
HeLa cells
mEAK7-mCherry
10 kDa FITC-dextran
Merge
C
HEK293T lysosomes steady state pH
ns
pH
7
6
5
4
3
Wildtype
mEAK7 unlabelled overexpressed
D
RAW phagosomes steady state pH
ns
pH
6.0
5.5
5.0
4.5
4.0
3.5
Wildtype
mEAK7 unlabelled overexpressed

Figure 3

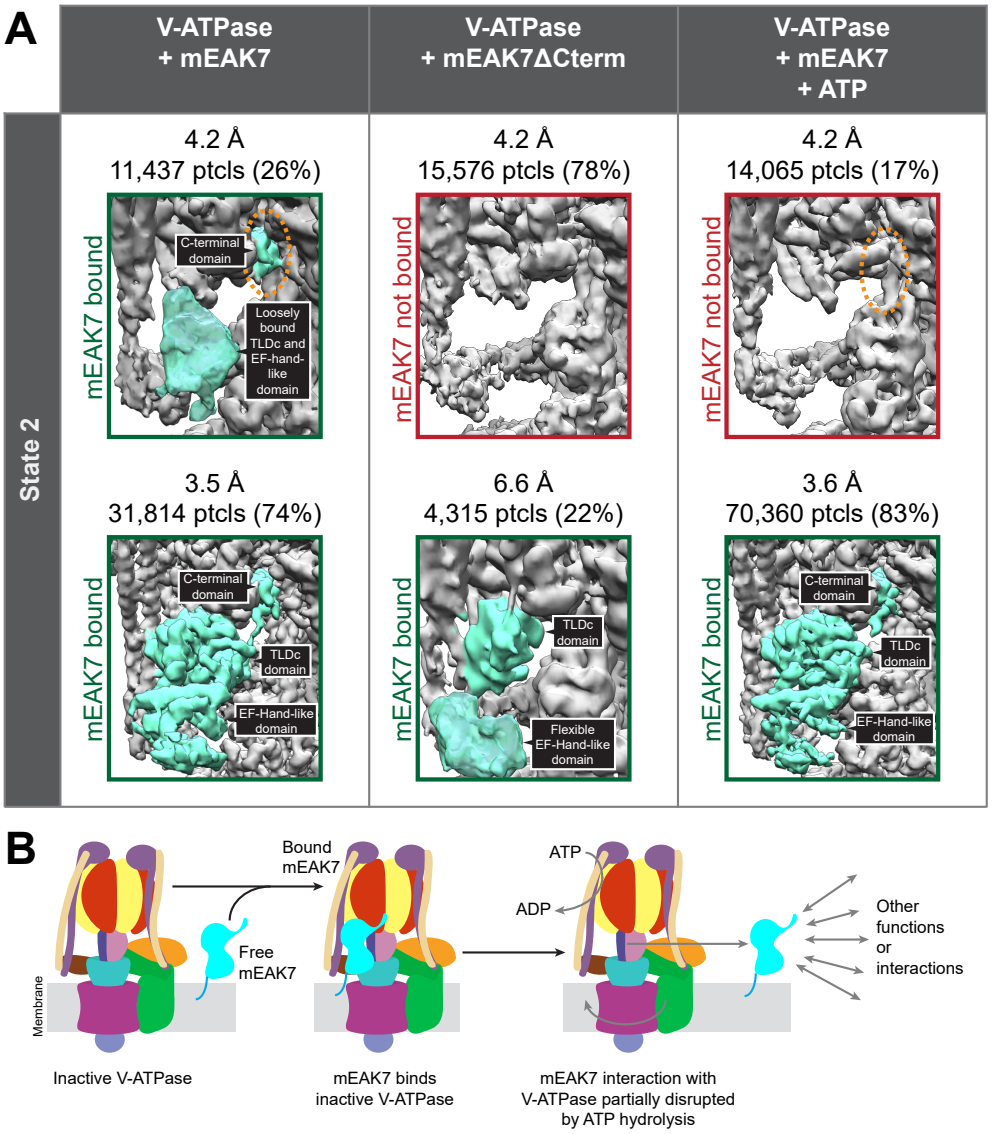
A
V-ATPase + mEAK7
V-ATPase + mEAK7ΔCterm
V-ATPase + mEAK7 + ATP
State 2
4.2 Å
11,437 ptcls (26%)
mEAK7 bound
C-terminal domain
Loosely bound TLDc and EF-hand-like domain
4.2 Å
15,576 ptcls (78%)
mEAK7 not bound
4.2 Å
14,065 ptcls (17%)
mEAK7 not bound
3.5 Å
31,814 ptcls (74%)
mEAK7 bound
C-terminal domain
TLDc domain
EF-Hand-like domain
6.6 Å
4,315 ptcls (22%)
mEAK7 bound
TLDc domain
Flexible EF-Hand-like domain
3.6 Å
70,360 ptcls (83%)
mEAK7 bound
C-terminal domain
TLDc domain
EF-Hand-like domain

B
Membrane
Free mEAK7
Bound mEAK7
ATP
ADP
Other functions or interactions
Inactive V-ATPase
mEAK7 binds inactive V-ATPase
mEAK7 interaction with V-ATPase partially disrupted by ATP hydrolysis

Figure 4

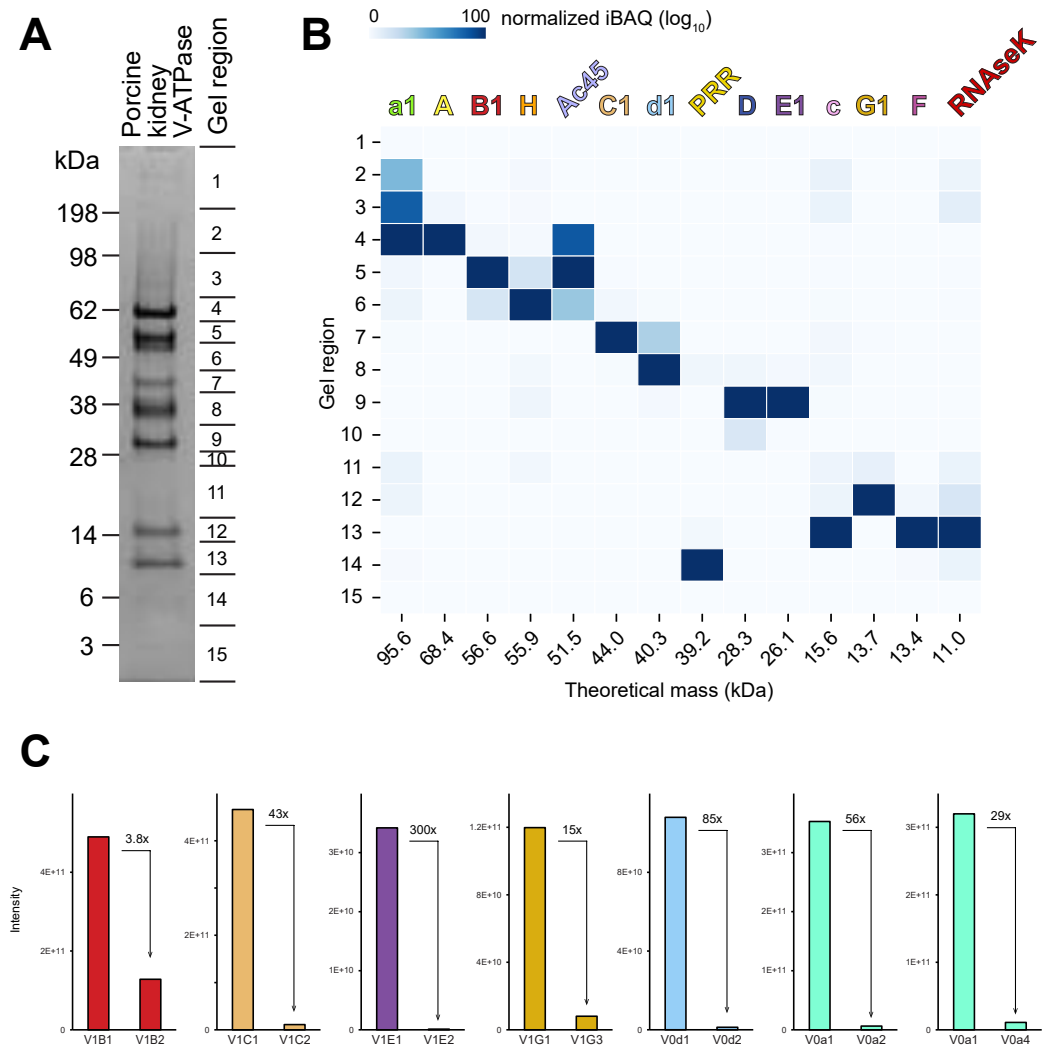

Supplementary Figure 1

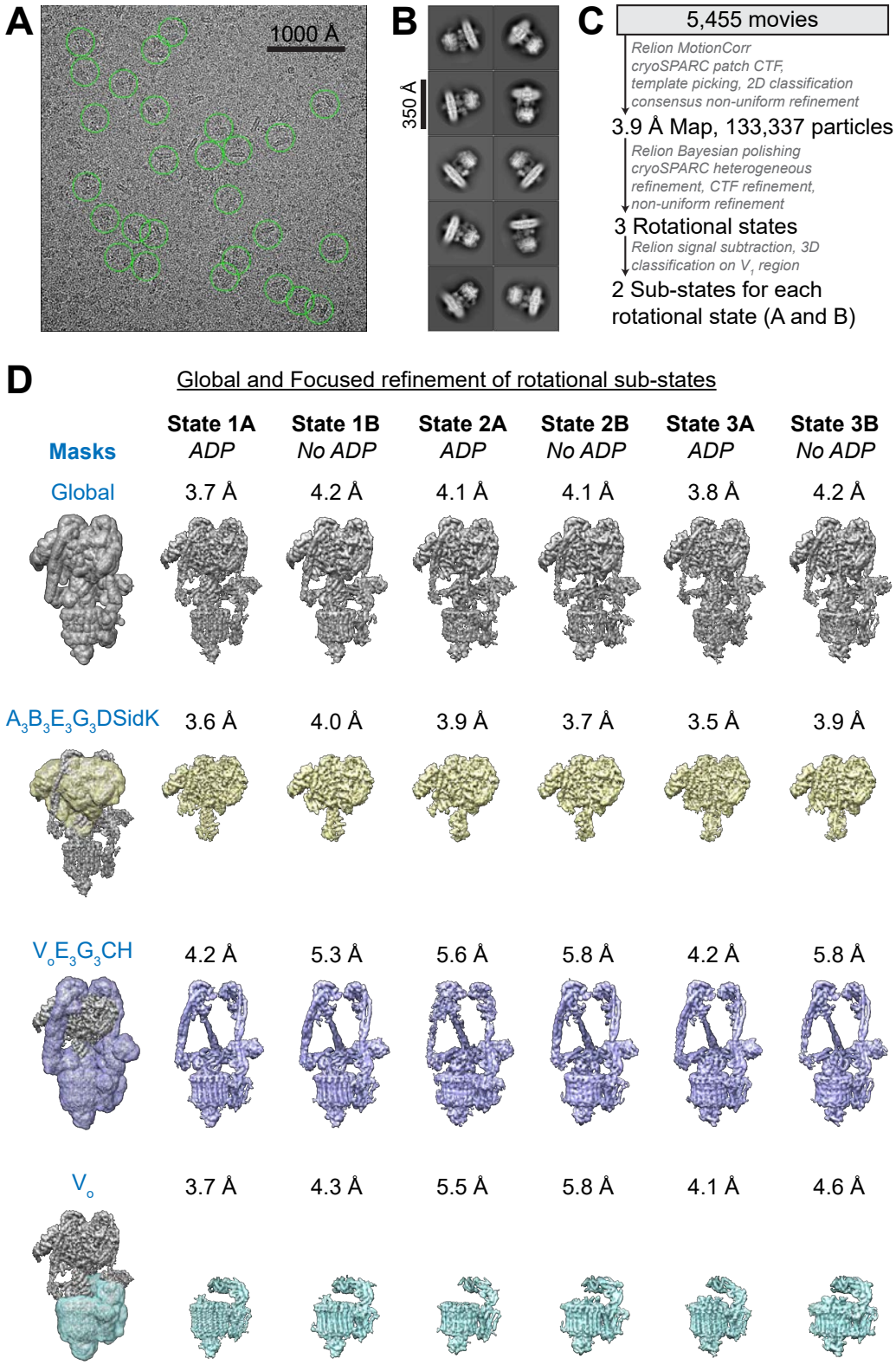

Supplementary Figure 2

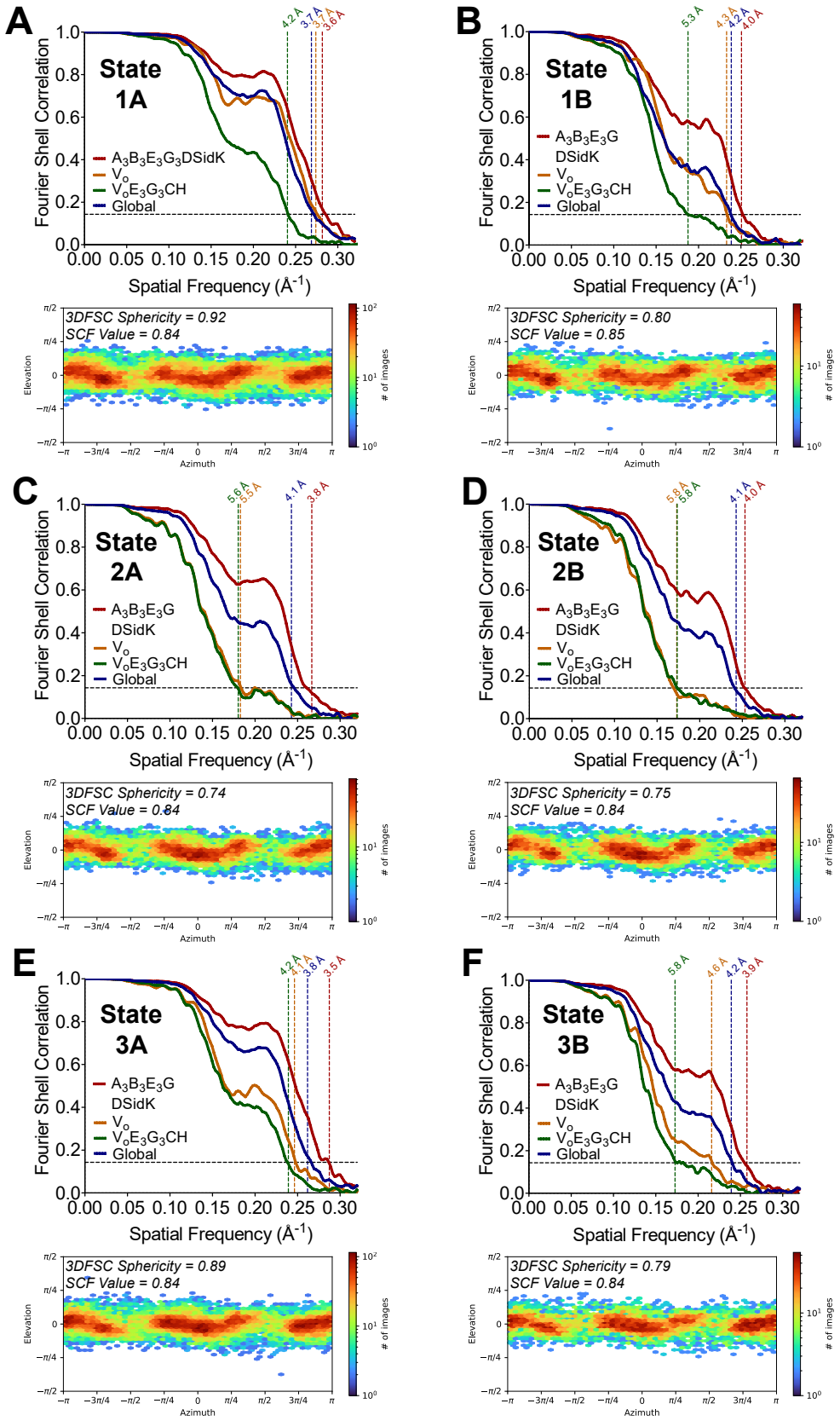

Supplementary Figure 3

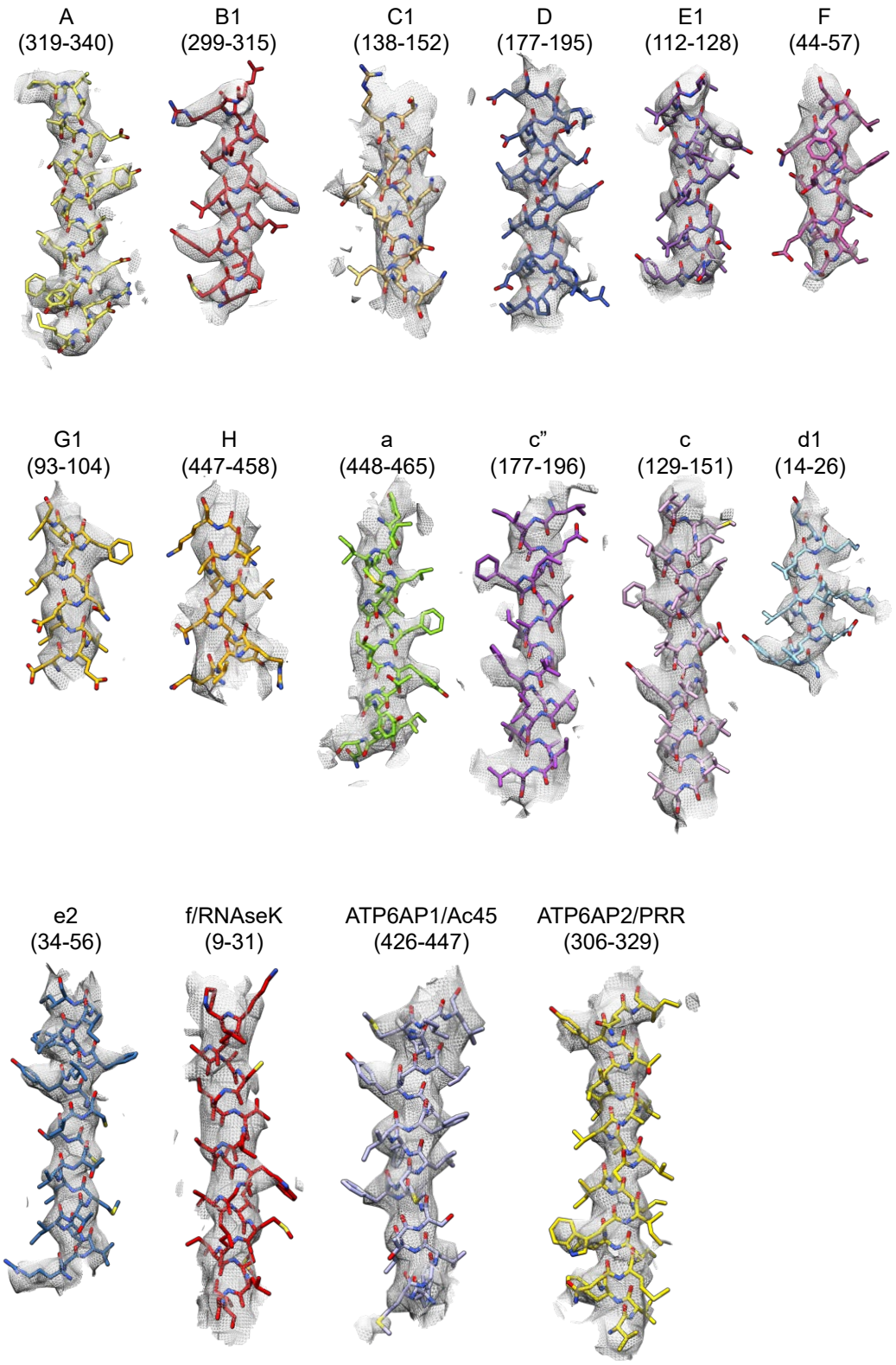

Supplementary Figure 4

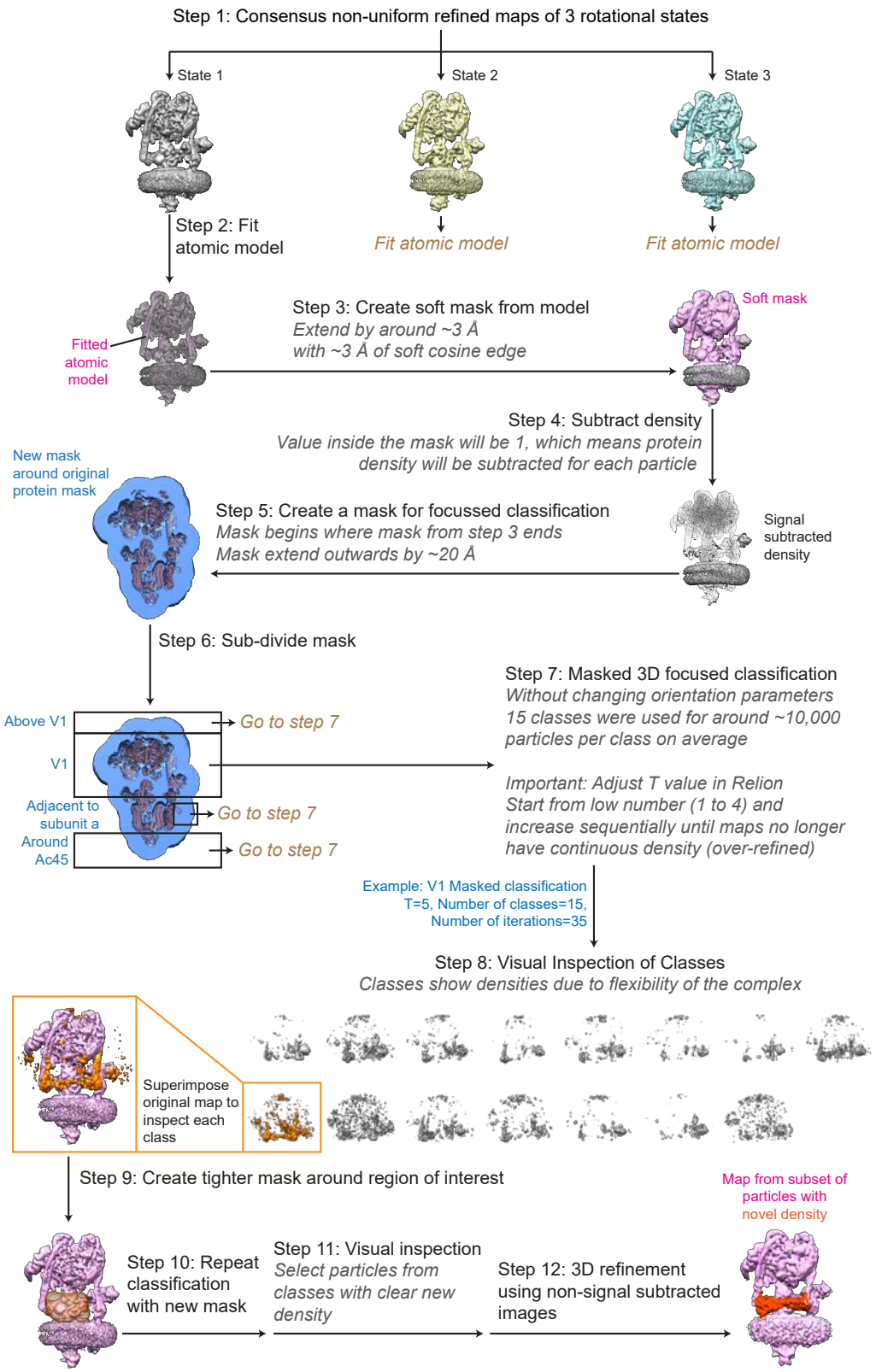

Supplementary Figure 5

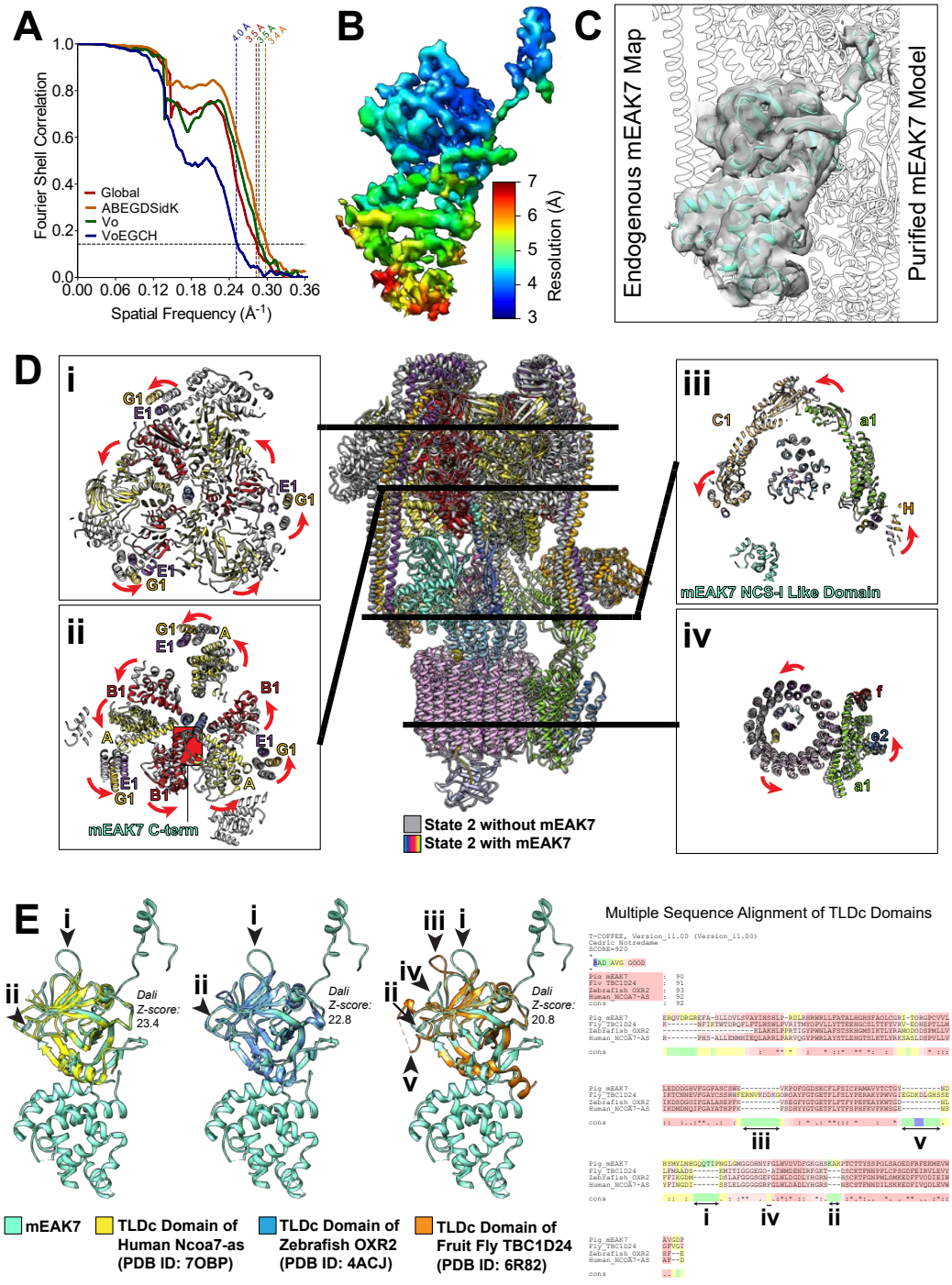

Supplementary Figure 6

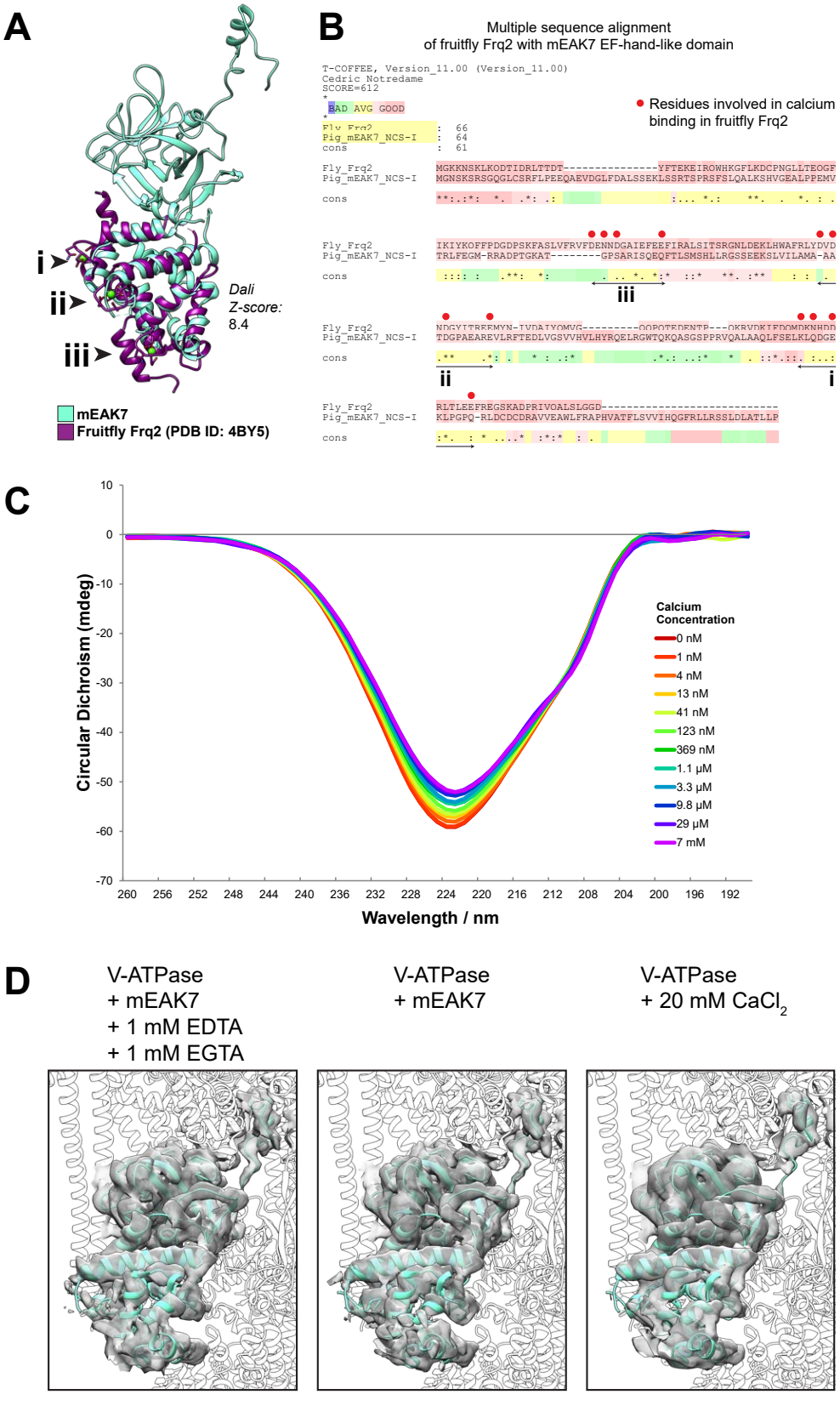

Supplementary Figure 7

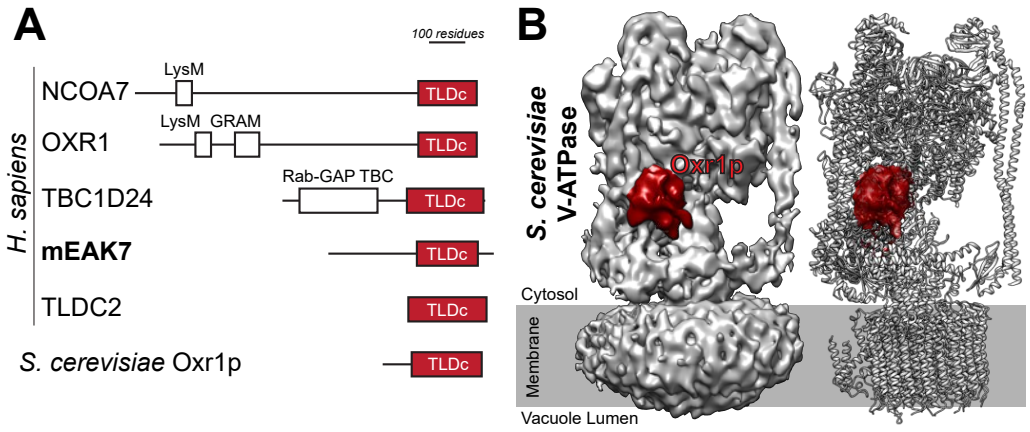

Supplementary Figure 8

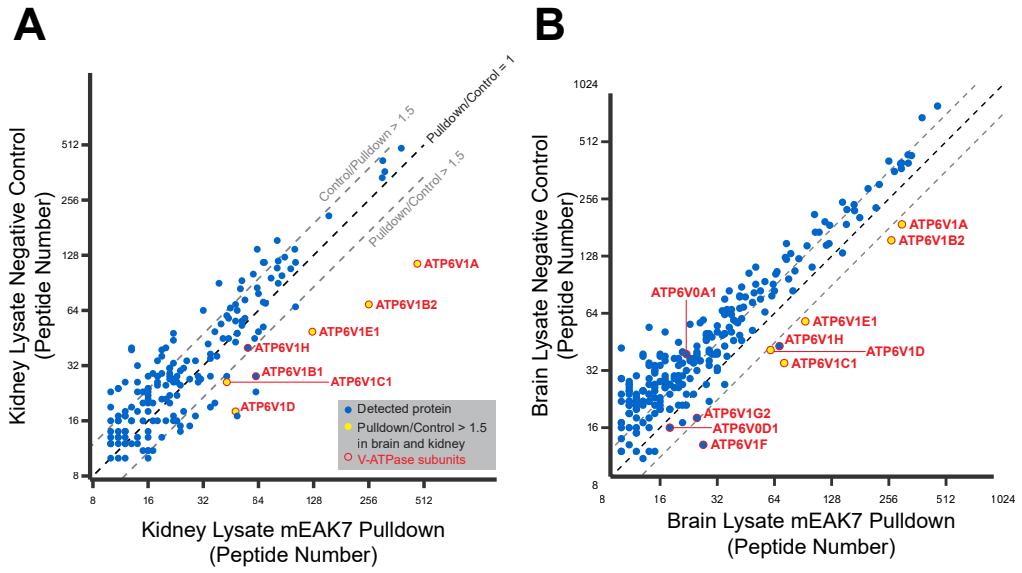

Supplementary Figure 9